LAWRENCE
LIVERMORE
NATIONAL
LABORATORY

LLNL-JRNL-534951

Thermo-mechanical modeling of laser-induced structural relaxation and deformation of SiO2 glass

R. M. Vignes, T. F. Soules, J. S. Stolken, R. R. Settgast, S. Elhadj, M. J. Matthews

March 5, 2012

Journal of the American Ceramic Society

Disclaimer

This document was prepared as an account of work sponsored by an agency of the United States government. Neither the United States government nor Lawrence Livermore National Security, LLC, nor any of their employees makes any warranty, expressed or implied, or assumes any legal liability or responsibility for the accuracy, completeness, or usefulness of any information, apparatus, product, or process disclosed, or represents that its use would not infringe privately owned rights. Reference herein to any specific commercial product, process, or service by trade name, trademark, manufacturer, or otherwise does not necessarily constitute or imply its endorsement, recommendation, or favoring by the United States government or Lawrence Livermore National Security, LLC. The views and opinions of authors expressed herein do not necessarily state or reflect those of the United States government or Lawrence Livermore National Security, LLC, and shall not be used for advertising or product endorsement purposes.

Thermo-mechanical modeling of laser-induced structural relaxation and deformation of SiO_2 glass

Ryan M. Vignes, Thomas F. Soules, James S. Stolken, Randolph R. Settgast, Selim Elhadj and Manyalibo J. Matthews*

National Ignition Facility and Photon Sciences, Lawrence Livermore National Laboratory
7000 East Avenue, Livermore, California 94550

Abstract

A fully-coupled thermo-mechanical finite element method modeling the deformation of SiO_2 due to infrared laser (IR) heating is presented. Direct measurement of the transient, non-uniform surface heating profiles based on *in-situ* micro-pyrometry was used to first validate a non-linear thermal transport model. Contributions from convection and radiation were found to be negligible from 293 to 3000 K, while evaporative cooling dominated only above ~2500 K. Densification due to structural relaxation above the glass transition point was modeled using the Tool-Narayanaswamy (TN) formulation for the evolution of structural relaxation times and fictive temperature. TN relaxation parameters were derived from spatially-resolved confocal Raman scattering measurements of Si-O-Si stretching mode frequencies. Together, these thermal and microstructural data were used to simulate fictive temperatures which are shown to scale nearly linearly with density, consistent with previous bulk densification measurements from Shelby *et al*. The densification, along with the thermal expansion occurring in the liquid and solid SiO_2 phases lead to residual stresses and permanent deformation in the SiO_2 sample which could be quantified. However, experimental surface deformation profiles between 1700 and 2000 K could only be reconciled with our simulation by assuming a roughly 2x larger liquid thermal expansion for SiO_2 with a temperature of maximum density (TMD) ~150 K higher than previously estimated by Bruckner *et al*. The resulting stress fields calculated for IR laser heating agreed well with critical fracture and birefringence measurements, thus enabling accurate material response prediction for SiO_2 laser processing conditions of practical interest.

Keywords: laser texturing, structural relaxation, thermoplasticity, thermal expansion, fictive temperature

**Corresponding author, ibo@llnl.gov*

I. INTRODUCTION

Localized micro- and nano-patterning of glasses using focused laser beams has been exploited for a wide range of scientific and industrial applications (Barborica et al., 1994; Bass et al., 2010; Bennett et al., 1999; Hnatovsky et al., 2006; Horstmann-Jungemann et al., 2009; Kim et al., 1995; Koshiba et al., 2007; Sorescu and Knobbe, 1994; Wakaki et al., 1998). Fundamental to these applications is an accurate description of the laser-induced spatially-varying thermal history of the material and the constitutive equations which dictate material response. For example, the nonlinear dependence of ablation rate (Mendez et al., 2006), thermocapillarity (Anthony and Cline, 1977), structural relaxation (Scherer, 1990) and residual stress (Dahmani et al., 1998; Rubenchik and Feit, 2003) on temperature requires sensitive tuning of laser parameters to achieve optimal processing. The temperature distribution within the material due to laser heating can be calculated by solving the heat equation while the constitutive model used in the equilibrium equation lends insight into material motion and the development of stresses. In terms of laser sources, most common for laser pattering/machining are Nd:YAG (1.064 μm) and CO_2 (10.6 μm) lasers, both in pulsed and continuous mode (CW) temporal format. Due to their ready availability and the relatively short absorption length of amorphous SiO_2 at 10.6 μm (3~40 μm), CO_2 lasers are typically used for silica-based glass laser processing (Bennett and Li, 2001; Mendez et al., 2006). For laser-driven temperature changes up to the glass transition point (T_g ~ 1400 K, depending on OH content), the material responds thermoelastically with little hysteresis in physical properties within 'laboratory' time scales (≤100 s).

In the glass transition region ($T \sim T_g$), amorphous SiO_2 behaves viscoelasticly leading to stress relaxation, but also undergoes *structural* relaxation, leading to fundamental changes in Si-O bonding arrangements thereby affecting the final material properties (Scherer, 1986). Structural relaxation in high purity SiO_2 glass can be observed most profoundly in the temperature dependence of the specific volume, as shown in Fig. x. If thermally cycled over sufficiently long times (~days-weeks), the glass transition can be observed below 1400 K and has lead to the recent identification of an anomalous density minimum in the low density amorphous (LDA) phase of SiO_2(Sen et al., 2004). At higher temperatures, and over shorter time scales commensurate with laser heating, a high density amorphous (HDA) phase has been known for some time(Angell and Kanno, 1976; Bruckner, 1970), though the precise temperature of maximum density (TMD) is still somewhat unclear (Shelby, 2004). Nonetheless, at sufficiently high temperatures and/or long time scales, the silica essentially behaves as a viscous fluid and the thermal expansion coefficient changes from that of one for a metastable "solid" to that of an equilibrium "liquid". At the end of a laser pulse, the silica can cool rapidly through conduction, driven by the high thermal gradients typical of focused laser heating. A rapid quench may produce a pit due to the volumetric contraction of the liquid, or it may result in a protrusion due to freezing in the constrained shape of the heated region or a combination of both depending on the thermal history and details of the liquid-like and solid-like thermal expansion coefficients. Even in the absence of high temperature (T>2000 K) processes such as capillarity, Marangoni stresses or evaporation, laser-induced morphology changes can still be dramatically changed due to stress and volume relaxation effects leading to several interesting micro- and nano-patterning applications (Bennett et al., 1998; Kitamura et al., 2003; Veiko et al., 2005). On the other hand, rapid quenching of the material can result in large, undesirable residual stresses developed both at the surface and within the bulk of the SiO_2.sample. Therefore, understanding both the stress and structural relaxation phenomena of silica is necessary in order to minimize the resulting residual stresses and to help create and shape a desirable surface profile.

Interestingly, while a large body of theoretical and experimental work exists on bulk relaxation processes of silica-based glasses on macroscopic length scales (Narayanaswamy, 1971; Scherer, 1993; Tool, 1945), few glass relaxation studies examine in detail the rapid, high temperature micro-scale heating associated with laser irradiation(Bennett and Li, 2001). Conversely, although several laser-heating studies have extensively covered laser-matter interactions including complex melt pool dynamics(Han et al., 2005; Kaplan and Tokarev, 1999) and heat transport(von Allmen and Blatter, 1998),

few involve a complete depiction of both viscoelastic behavior and structural relaxation. In particular, since relaxation behavior and thus material properties are determined through heating and cooling rates, an accurate constitutive model is critical in the overall modeling of material response.

Experimentally, the uncertainty associated with the relevant material thermal properties at high temperatures (T~1800 K), makes direct *in situ* temperature measurements crucial for validation of laser-heating computational models. *Ex situ*, characterization of thermally-induced changes in the glass structure is also fundamental in that it allows one to establish an accurate relaxation model. Historically, vibrational spectroscopy (Agarwal et al., 1995; Galeener, 1982; Geissberger and Galeener, 1983; Matthews et al., 2010; McMillan et al., 1994; Ryu and Tomozawa, 2006) has been used to measure changes in phonon spectrum associated with 3- and 4-membered ring populations and/or shifts in O-Si-O bond lengths and angles, all of which have been calibrated to changes in fictive temperature. However, despite the numerous studies of structural relaxation in bulk-heated silica-based glasses, only recently (Bennett and Li, 2001; Matthews et al., 2010; Zhao et al., 2004) have studies attempted to address the application of standard relaxation models to fused silica glass treated with localized laser heating.

The article describes a method in which the coupled heat transfer and equilibrium equation are solved, in conjunction with a constitutive model capable of evolving stress and structural relaxation phenomena, allowing residual stresses and a deformed surface profile to be predicted. It is shown that a complete description of the interaction of these three physical phenomena is required in order to obtain agreement with experiment. Stress relaxation is modeled using the phenomenological Tool-Narayanaswamy formalism. Due to the high temperatures and rapid heating/cooling of the laser treatment of the surface, thermal-mechanical constitutive properties must be extrapolated beyond the temperature range over which they have been measured. The simulated temperatures are compared with experimental measurements of the surface during the heating process, while experimental fictive temperature measurements taken using bulk IR and spatially-resolve confocal Raman techniques are used to derive structural relaxation parameters. Using both reference and experimental data we propose a complete liquid-solid thermal expansion for amorphous SiO_2. The final surface profile is compared with the measured experimental profile obtained using an interferometric microscope. This coupled, multi-physics model reproduces the experimental results well and lends further insight into the behavior of solid and liquid silica under conditions where experimental measurements were not previously accessible.

II. MODEL

Analytic solutions for simplified laser heating profiles and constant material properties which are independent of temperature have been obtained in (Bouchut et al., 2004; Lax, 1977, 1978). However analytical solutions involving non-linear, temperature dependent material properties and complex laser heat input, are difficult if not impossible to obtain. As an alternative approach, a multiphysics finite-element model was developed to analyze the heat transport, structural relaxation, material motion and residual stress in a laser-heated silica disk. In solving multiphysics problems, two solution methods exist: a monolithic solve and staggered, operator split solve (fractional step method). While a monolithic solve is fully coupled and able to determine all the physical unknowns (temperature, displacement, etc.,) at once, it can be subject to numerical instabilities and requires more computational effort than an operator split solve. An operator split solve obtains the solution to a single physics field at a time. Once a solution to that field has been obtained, time is held fixed, material properties are updated based on the updated physic's state and the next physic's field is solved. With time held fixed, iterations between the physics' field continue until all governing equations are satisfied. In the simulations discussed below, the operator splitting method has been used, as it tends to be the preferred solution method (Armero and Simo, 1992, 1993; Yanenko, 1971) . Due to the long time scales of the simulation, time-stepping was performed using the implicit Hilbert-Hughes-Taylor time integration method (Hilber et al., 1977). During the initial simulations, complete iterations between the heat equation and balance of momentum were performed;

however, it was later determined that the same solution could be more rapidly obtained without the iterations between the physics' fields if the temperature change per timestep was restricted to a sufficiently small value, which prevent large changes in the material properties.

A. Geometry and Energy Deposition

A spatially-symmetric Gaussian-shaped laser beam was used to heat a cylindrically shape disk 50.4 mm in diameter and 10 mm thick. A 2D axisymmetric geometry can then be used to describe the volumetric energy deposition into the silica as a function of time *t*, radial position from the center of the beam, *r*, and depth into the sample, *z*:

$$Q(r,z,t,T) = \frac{P(t)\cdot\gamma(T)}{\pi\cdot r_0^2}\cdot\exp(-\gamma(T)\cdot z)\exp\left[-2\left(\frac{r}{r_0}\right)^2\right]. \qquad (1)$$

In Eq.(1), $P(t)$ is the time-dependent laser power reduced by Fresnel reflection at the surface, $\gamma(T)$ is the temperature dependent laser absorption coefficient and r_0 is the $1/e^2$ radius of the Gaussian beam. The reflectivity at normal incidence of fused silica at 10.59 μm is 15% and varies less than 1% over the temperatures ranges considered in our experiments (Philipp, 1985). The temperature-dependent absorption coefficient for the 10.59 μm radiation emitted by a CO_2 laser was measured by McLachlan and Meyer to vary as $\gamma(T)=1.71\ mm^{-1} + [9.15x10^{-2}\ mm^{-1}K^{-1}]T$ between 298 K and 2073 K (McLachlan and Meyer, 1987). For transient analysis the energy deposition was sufficiently resolved within the laser absorption depth (4 μm at 2000 K) by using a split operator algorithm and a highly non-uniform finite-element mesh of 22,000 elements. The element size ranged from 2x2 μm directly below the laser to 30x30 μm at the opposite boundary of the sample.

B. Heat Transport

With the volumetric heat source, *Q*, defined above, the nonlinear heat equation can then be described as

$$\rho(T)\cdot C_v(T)\cdot\frac{\partial T}{\partial t} - \nabla\cdot(\kappa(T)\cdot\nabla T) = Q(r,z,t,T)$$

(2)

where ρ, C_v and κ are the mass density, heat capacity at constant volume and thermal conductivity, respectively. The operator split requires the use of C_v, which can be related to C_P through well-known thermodynamic relations.

Although there is only a slight variation in ρ with temperature, both $C_p(T)$ and $\kappa(T)$ vary appreciably from room temperature up to ~2000 K. In particular, because $C_P(T)$ and $\kappa(T)$ increase by almost a factor of two between 300 and 2000 K, the surface cooling rate at the laser center, - varying approximately as $\sqrt{t/\kappa C_P}$ (von Allmen and Blatter, 1998) - will be over-estimated by a factor of two if room temperature values are assumed. C_P data was obtained for both Heraeus Homosil 102 (Heraeus) and Corning 7980 (Corning)(Corning)(Corning)(Corning)(Corning)(Corning)(Corning)(Corning)(Corning)(Corning) glass up to 900 K, and was then extrapolated up to 2000 K using model fits. As first shown by Smyth *et al.*, $C_v(T)$ of bulk silica can be well-represented by the Einstein individual oscillator model up to ~1500 K, using phonon mode frequencies (expressed in temperature) θ_{Si} = 1200 K, θ_T = 1100 K and θ_L = 370 K. We found that a two oscillator fit to C_P data sufficiently described the data (θ_T = 915 and θ_L = 239 K) and used the fit to extrapolate to higher temperatures. As further confirmation, the fitted C_v is indeed observed to asymptote to within 5% of the classical Dulong and Petit limit of ~3R where R is the universal gas constant (though at higher temperatures this limit must be modified by contributions from

anharmonic and configuration terms). The temperature dependence of $\rho(T)$ is discussed in more detail below with regard to thermal strains, but in terms of thermal transport, variation over T due to changes in ρ were found to be negligible (<1%). Therefore, in the calculations for $T(r,z,t)$ that follow, density is taken as contanst, $\rho(T)=\rho_0$.

The thermal conductivity of bulk fused silica has also been studied extensively (Kingery, 1961; Wray and Connolly, 1959), and data was available from the aforementioned manufacturers as well. However, it is important to note when citing either sources of κ data that bulk measurements, particularly at high temperature, often include contributions from radiation and do not represent the intrinsic phonon conductivity (Elhadj et al., 2010; Mann et al., 1992). Therefore we considered only low temperature (T<700 K) data from Corning and Heraeus, and extrapolated the data using the thermal conductivity for isotropic bulk materials based on kinetic theory,

$$k(T) = \frac{1}{3} r \times C_p(T) \times v(T) \times L(T) \tag{3}$$

where $v(T)$ is the mean phonon velocity and $\Lambda(T)$ is the phonon mean free path. The mean phonon velocity for fused silica has been determined up to 2300 K by (Polian et al., 2002) using Brillouin scattering measurements. Unfortunately, data on Λ is relatively scarce over the temperature range of interest. In contrast to crystal systems where Umklapp-scattering leads to an appreciable temperature dependence, the high amount of disorder in glasses tends to dictate Λ, leading to a relatively weak decrease over T, especially at high temperatures. We therefore constructed a model for $\kappa(T)$ based on $\Lambda(T) = \Lambda_0 + \Lambda_1/T$ and use the mean free path fitting parameters to extend $\kappa(T)$ from 300 to 2000 K. As shown in Fig. 2(b), the derived phonon mean free path decreases and asymptotically approaches a value close to the size of the molecular SiO_2 unit (~0.4 nm). For the finite element simulations that follow, piece-wise linear approximations to C_P (see Appendix) and κ are constructed. Precise values of the material thermal properties were tabulated and can be found in our associated Supplemental Material publication.

Heat transfer boundary conditions for laser-heating problems typically include surface convection, radiation, and evaporative cooling but are highly dependent on the temperature range of interest. In fact, most of the heat loss from the laser treated spot is through conduction into the bulk. It can be shown that the large temperature gradients associated with laser heating of highly absorbing media result in radiation contributions to the bulk thermal conductivity and radiation loss from the surface that are negligible (Elhadj et al., 2010; Shestakov et al., 2011). Natural convection from the surface is given for our geometry by $q_{conv} = 1.823\times10^{-6}(T_{surf} - T_\infty)^{1.293}$ W/m^2 (Churchill and Chu, 1975), and is estimated to be roughly an order of magnitude smaller than radiation losses. This leaves evaporation as the dominant boundary loss and conduction as the dominant loss in the bulk. Figure 3 compares the relative contributions of the four transport mechanisms up to 3000 K, estimated analytically for a steady-state 1mm beam over a range of peak powers. As shown, until peak temperatures approach the boiling point of SiO_2 (~2500 K), heat is lost largely through conductive cooling. Thus, for the laser experiments discussed in this paper, surface heat loss boundary conditions have only a small effect on the results in the temperature range < 2500 K. The model results had little dependence on the remaining sample boundary conditions (interfaces not exposed to laser light) which were assumed adiabatic.

C. Momentum Balance and Constitutive Response

Once the laser deposits heat into the silica, thermal expansion and contraction will cause the material to deform and stress to develop. The deformation and stress are obtainable by solving the momentum conservation equation

$$\nabla \cdot \boldsymbol{\sigma} + \mathbf{b} = \rho \frac{\partial^2 \mathbf{u}}{\partial t^2}, \tag{4}$$

where $\boldsymbol{\sigma}$ is the Cauchy stress tensor, **b** are applied body forces (zero for this particular case of laser heated silica), and **u** are the displacements. A constitutive model, which describes material behavior based on empirical or phenomenological observations, is used to relate the deformation to the stress state. For the silica constitutive model, the deformation was decomposed into a deviatoric component described by a viscoelastic strength model and a volumetric component described by an equation of state.

C.1 Viscoelastic strength model

As silica is an amorphous solid which lacks long range order in its atomic structure, a purely elastic response in insufficient to describe the deformation; a viscoelastic response is required to allow for the time-dependent stress and strains. A multi-element Maxwell spring model can sufficiently capture this phenomenon. Casting the Maxwell model in terms of deviatoric stress rate, $\dot{\mathbf{s}}$, and strain rate, $\dot{\varepsilon}$, results

$$\frac{\dot{\mathbf{s}}^{(k)}}{2G_k} + \frac{\mathbf{s}^{(k)}}{\eta_k} = \dot{\boldsymbol{\varepsilon}}, \tag{5}$$

where (k) indicates the kth Maxwell element, G is the shear modulus, η is the viscosity, and the deviatoric stress is related to the Cauchy stress as $\mathbf{s} = \boldsymbol{\sigma} - \frac{1}{3}\operatorname{tr}\boldsymbol{\sigma}\,\bar{\mathbf{I}}$. Upon integrating Eq. (5), the stress at a future time can be obtained based on the current stress, current strain, and material properties as

$$\mathbf{s}^{(k)}_{t_n+\Delta t} = \eta_k (1 - e^{-c_k})\dot{\boldsymbol{\varepsilon}} + e^{-c_k}\mathbf{s}^{(k)}_{t_n} \tag{6}$$

where $c_k = \frac{\Delta t}{\tau_k}$ and $\tau_k = \frac{\eta_k}{2G_k} = \tau_{ok}\exp\left[\frac{\Delta H_k}{R}\frac{1}{T}\right]$. ΔH_k is the activation enthalpy for the kth Maxwell element and τ_k is the relaxation time and produces temperature dependent stresses when H_k is non-zero.

C.2 Equation of state model

An equation of state (EOS) is required to relate state variables used in our finite element code in order to be self-consistent under operator split conditions. For the volumetric deformation of silica, the EOS must account for both temperature and pressure contributions to the change in volume. Moreover, we will seek to relate an EOS for silica to material properties that are known or measurable in the region of phase space relevant to laser heating. A piece-wise construct of the Gibbs free energy, $\mathcal{G}$, is used here to describe an isothermal, isobaric thermodynamic system and can be written as

$$\mathcal{G}(P,T) = \mathcal{G}_0 + \left(c_0 - S_0 - \frac{1}{2}c_T(T+T_0)\right)(T-T_0) - T\,(c_0 - c_T T_0)Log\left(\frac{T}{T_0}\right),$$
$$+\left(\left(\frac{k_0 + k_T(T-T_0)}{K_T(P,T)}\right)^{\frac{1}{K_p}-1} - 1\right)\frac{(k_0 + k_T(T-T_0))}{K_p - 1}V_1 \tag{7}$$

and is defined in detail in the appendix. By taking appropriate derivates of the Gibbs function, the isothermal bulk modulus, $K_{\text{iso}} \equiv \left(-\left.\frac{\partial^2 \mathcal{G}}{\partial V^2}\right|_T\right)$, specific heat, $C_P \equiv \left(T\left.\frac{\partial^2 \mathcal{G}}{\partial T^2}\right|_P\right)$, and the coefficient of thermal expansion, $\alpha \equiv \left(\frac{1}{V}\left.\frac{\partial^2 \mathcal{G}}{\partial P\,\partial T}\right|_{PT}\right)$, can be obtained at constant pressure, P_o, and fit to available data. The temperature range of interest may be divided into a suitable number of segments. Using this approach, the bulk modulus, heat capacity, and thermal expansion coefficients are then piece-wise linear functions of temperature on the reference iso-bar, P_o. This facilitates describing complex temperature dependent constitutive behavior to any desired degree of accuracy while ensuring the potential nature of thermo-elasticity. The method also prevents hysteresis of arbitrary closed-paths in strain or temperature and thereby ensures consistency of thermally induced residual stress estimates. Figure 4(a) displays K_T, the temperature-dependent bulk modulus, and K_P, the pressure-dependent bulk modulus, both plotted as a function of temperature and derived from (Polian et al., 2002). Fig. 4(b) contains the sum of these bulk moduli, yielding the isothermal bulk modulus K_{iso}.

Thermal expansion of silica glass is moderately dependent upon the glass type (I-IV) and fictive temperature (Bruckner, 1970; Kuhn and Schadrack, 2009; Shelby, 2004). Directly accounting for this entails incorporating the fictive temperature into the above expression for the Gibbs free-energy. This complication was avoided by estimating a mean value of thermal expansion for the solid over a range of fictive temperatures. Using the data plotted in Fig. 21 of Bruckner, the thermal expansion of type II silica was estimated as both a function of temperature and fictive temperature. The fictive temperatures reported in (Bruckner, 1970) were corrected using Fig. 2 of Shelby, which reduces the reported value of 1530K to 1415K, thereby increasing the sensitivity of thermal expansion to fictive temperature. The mean thermal expansion coefficient at any give temperature was estimated by taking the arithmetic mean of the fictive temperature from 1400-1900 K.

Estimating the thermal expansion of sub-cooled liquid silica is complicated by the presence of a liquid-liquid phase transition as described in (Sen et al., 2004). However, in that work, the authors studied silica synthesized from $SiCl_2$ (essentially type IV), which precludes using the measured values of thermal expansion in this study due to the well-documented dependence of thermal expansion on dissolved chlorine. In the absence of measured data, the thermal expansion of liquid type II silica was inferred from surface profile measurements described in section IV.B below. The temperature dependence of the sub-cooled liquid's thermal expansion coefficient is assumed to be linear and the coefficients were adjusted to achieve agreement with experiment. This fitting process is highly constrained by the measured surface profiles, the measured fictive temperature distributions, and by fitting two parameters, slope and intercept, to four independent experimental conditions.

D. Volumetric Thermal Strain and Silica Fictive Temperatures

The main effect of laser heating is to produce a thermal strain that serves as the load to the equilibrium equation. At temperatures below the glass transition region, thermoelastic strain in heated silica glass is well-described by a solid thermal expansion coefficient. However the form of glassy SiO_2 thermal expansion in the liquid-like state of the glass is still a matter of debate (Bruckner, 1970; Sen et al., 2004; Shelby, 2004) with complications arising from silica undergoing both temperature-dependent stress *and* structural relaxation. In this paper, structural relaxation is handled using the Tool-Narayanaswamy phenomenology (Narayanaswamy, 1971; Tool, 1946), which assumes that a glass has properties that can be measured over a temperature range in two states: the equilibrium liquid state and the metastable solid state (the thermodynamically stable crystalline solid state not being reached unless the glass devitrifies). The fictive temperature, T_f is defined as the temperature of the melt that is in structural equilibrium with – or structurally equivalent to the meta-stable solid. The fictive temperature depends only on the thermal history of the sample, and is interpreted in terms of phase transitions as a single order parameter. For example, if the glass is cooled at a faster rate, a given physical property will "freeze-in" from the liquid to the solid at a higher temperature. In the Tool-Narayanaswamy formalism, the fictive temperature is given by

$$T_f = T - \int_0^t M_V\left[t, t', T(t')\right] \times dT(t') \tag{8}$$

where $M_V\left[t, t', T(t')\right]$ is the relaxation function and is frequently represented as either a stretched exponential with a Kohlrauch exponent β, or a sum of exponentials with a relaxation time τ_V that has an Arrhenius dependence on both the temperature and fictive temperature:

$$M_V(t) = \exp\left[\frac{-t}{\tau_V}\right]^{\beta} = \sum_{i=1}^{n} c_i \exp\left[\frac{-t}{\tau_V}\right] \tag{9}$$

$$\tau_V = \tau_{V\infty} \exp\left\{\frac{\Delta H}{R}\left[\frac{x}{T} + \frac{(1-x)}{T_f}\right]\right\} \tag{10}$$

In Eq. (10), ΔH is the activation enthalpy for relaxation , τ_{ref} is a relaxation time measured at T_{ref} and $0<x<1$ divides the activation energy between the thermodynamic temperature and the fictive temperature. The values of c_i may be chosen to fit the stretched exponential although in the case of high purity silica, recent studies have shown that a single exponential suffices.(Tomozawa et al., 2008) For the case of single exponential relaxation, the change in T_f over a given timestep Δt is given by

$$\Delta T_f = \frac{T - T_f}{\tau_V\left(T, T_f\right)} \Delta t. \tag{11}$$

(Markovsky and Soules, 1984) present an unconditionally stable numerical method for solving the differential form of Eqs. (8) and Eq. (11) so that starting from a glass of known fictive temperature the change in fictive temperature, ΔT_f, can be computed even though the relaxation times, $\tau_V\left(T, T_f\right)$, given by Eq. (9) change rapidly with T and T_f in the glass transition region:

$$T_f(t+\Delta t) = \frac{T(t)\cdot\left[\Delta t / \tau_V\left(T(t+\Delta t), T_f(t)\right)\right] + T_f(t)}{1 + \left[\Delta t / \tau_V\left(T(t+\Delta t), T_f(t)\right)\right]}. \tag{12}$$

The change in volumetric strain can then be calculated for each time step as long as both the solid and liquid volume thermal expansion coefficients, $\alpha_s(T)$ and $\alpha_l(T)$, are known(Soules et al., 1987):

$$\Delta\varepsilon^{th} = \frac{1}{3}\frac{\Delta V(T)}{V_0} = \alpha_s(T,T_f)\cdot\Delta T + \left[\alpha_l(T,T_f) - \alpha_s(T,T_f)\right]\cdot\Delta T_f . \tag{13}$$

E. Simulations Parameters

The parameters used in the above equations are given in Table I. The volumetric thermal expansion coefficients for the metastable solid were derived from recent OH- and T_f-dependent thermal expansion measurements up to ~1300 K (Kuhn and Schadrack, 2009). Despite inevitable water diffusion from the heated surface, the net change in OH content of our type II glass (~150 ppm wt.%) is not expected to change appreciably. However, for Corning 7980 (type III) a depletion of surface OH levels from ~800 ppm wt.% to less than ~500 ppm wt.% is known to occur near the surface following laser heating, so that near surface laser treated type III silica may behave more like that of a type II glass (Shen et al., 2010). Because our finite element formulation does not allow for an explicit dependence of the thermal expansion on T_f, an average curve was chosen based on fits to measured data. This yields somewhat higher values for solid silica thermal expansion at lower temperatures than traditional values, α_s ~ $1.65\text{x}10^{-6}$ < 773 K ultimately going to a zero thermal expansion coefficient near 2000 K, a temperature at which the solid would quickly relax to the equilibrium liquid.

Only one direct measurement of the liquid expansion coefficient was found (Sen et al., 2004) and only two data points on the curve fall in the temperature range of interest. The liquid thermal expansion coefficient as a function of temperature was indirectly inferred by (Bruckner, 1970) and (Shelby, 2004) from data on the density or specific volume at room temperature by rapidly quenching the glass from temperatures where the glass was in its equilibrium liquid state. Two assumptions were made in order to estimate a liquid curve from (Shelby, 2004): first that the fictive temperature is frozen in at the temperature at which the quench was started and second that the solid thermal expansion coefficient is independent of fictive temperature, allowing for a geometric construction suggested by (Douglas and Isard, 1951) to determine the liquid thermal expansion. However, as shown in Fig. 7(a) and further discussed in Section IV.C, there is not sufficient contraction in the liquid using either Bruckner's or Shelby's inferred liquid expansion curves to account for the depths of the laser induced pits.

The initial fictive temperature was determined from IR data as described in Section III and IV.B.. The enthalpy for shear stress relaxation and the pre-exponential factor $\tau_{S\infty}$ was obtained by fitting the Homosil published data for the viscosity and using $\tau = \eta/G$, where the viscosity was obtained for that of type II silica data from (Weiss, 1984). In keeping with previous work (Hau, 2011), the activation energy for structural relaxation is taken to be the same as for stress relaxation. $\tau_{V\infty}$, the pre-exponential for the structural relaxation time and x were treated as fitting parameters and were determined to provide a best fit to the measured fictive temperature profiles.

III. Experimental Methods

Polished UV-grade Heraeus Homosil 102 and Corning 7980 fused silica samples were used in the present study, 10 mm thick by 50.4 mm diameter round. As shown in Fig. 5, 10.6 μm continuous-wave (CW) light from a Synrad firestar V20 CO_2 laser was focused to a 0.40±0.02 mm $1/e^2$ diameter spot at the sample surface using ZnSe focusing elements. Beam power P, diameter d, and peak surface temperature T_{max} were all monitored in real time using a Mercury Cadmium Telluride (MCT) camera as described

elsewhere (Yang et al., 2009), and are tabulated along with exposure times in Table II. It is important to note that the micro-pyrometry used in the present study was restricted to 9 μm radiation, thus limiting the temperature measurement to within ~300 nm of the surface. Surface height maps were measured using a Zygo New View 100 white light interferometric microscope with 0.5 μm lateral and 1 nm axial spatial resolution. Total volume change at the laser treated regions was evaluated numerically using standard software. Visual inspection and optical microscopy (not shown) of the laser modified surface regions showed no evidence of laser ablation or redeposited material for the cases used in the analysis. Fictive temperature measurements were carried out using a custom 532 nm confocal Raman microscope previously described (Matthews et al., 2010) and applying the measured TO-mode frequency shift ν_{TO}~1060 cm^{-1} vs T_f from (Geissberger and Galeener, 1983). The axial and lateral spatial resolution of the Raman microscope was ~4 μm and ~2 μm respectively. Additionally, the IR absorption peak at ~2260 cm^{-1} of the starting substrates was measured using a commercial Fourier transform IR (FTIR) spectrometer and used to derive the bulk-averaged T_f after (Kakiuchida et al., 2003).

IV. Results and Discussion

A. Temperature distributions

The surface temperature profiles as measured using our MCT camera pyrometer at the time the laser was turned off after 5 seconds are shown in Fig. 5(a-d) for four different laser powers. Peak temperatures reach 97 % of their steady state value at < 0.6s and the rest of the temperature distribution has reached steady state at < 3s. Because of the limited resolution of our imaging system, the pixel count data was de-convoluted using the Wiener de-convolution method and a Gaussian point spread function. The latter was determined by imaging a focused spot of known radius and measuring the broadening caused by the limited resolution of the camera. The de-convolution function arrived at by this technique had a width at half maximum of 0.24 mm. In order not to block the laser beam, the spot had to be imaged on the camera at an off-axis angle resulting in a skewed pattern and so prior to the de-convolution the experimental data was azimuthally-averaged around the peak. The pixel data was converted to temperatures using an experimental emissivity curve (Rozenbaum et al., 1999) assuming that silica is a Planckian radiator and normalizing to a blackbody (Yang et al., 2009).

Figure 6 (a-d) shows the pixel count data from the camera converted to temperature, after being averaged and de-convoluted (symbols) and the calculated temperature obtained by solving Eq. (2) (lines). The calculated and experimental data obtained in this way show excellent agreement, and further shows the expected trend in peak temperature as the power of the laser is increased, as well as, the correct peak width. Measured time-dependent changes in the peak temperature (not shown) also agreed well with those from simulations. Ripples in the de-convoluted experimental data far from the peak temperature are artifacts due to the de-convolution. Although at large distances from the laser beam the average temperature remains at the initial room temperature, at distance less than 1.5 mm away from the laser beam the temperature is significantly higher than room temperature due to thermal conduction. As most of the material properties have a relatively strong temperature dependence, and these temperature dependent properties determine the fictive temperature material state, and are responsible for providing the loading which produce the stress and deformation, the computational model must be able to accurately predict the thermodynamic temperature field. From Fig. 6, it can be seen that the computational model does accurately capture the surface temperature field, in both peak temperature as well as the correct width and spatial decay in the temperature distribution.

B. Fictive temperature distributions

Figure 7 shows T_f as a function of radial position along the surface as determined through *ex situ* confocal Raman microscopy as described in the experimental methods section. The plots shown in Fig. 7 correspond 1:1 sample-wise with the measurements presented in Fig. 6, and were taken once the sample had returned to room temperature. Measured T_f values on the sample surface based on ν_{TO} observed in the Raman spectrum for r>0.1 ranged from ~1400 to ~1430 K, in good agreement with T_f=1420±4 K measured by FTIR of the pretreated bulk sample. For r<0.1, T_f smoothly varied to a maximum value (see Table II), increasing monotonically with increasing peak laser power. In all experimental curves, a slight inflection in $T_f(r)$ between 1600 and 1700 K can be observed, yielding direct indication of the temperature at which the relaxation time is roughly equal to the heating time, $\tau_V(T)$~5 s. For temperatures above this inflection, structural relaxation exceeds experimental time scales and the thermodynamic temperature T exceeds the final T_f. Conversely, below this point, T_f lags T due to relaxation times being much longer than the experimental time scale. To derive relaxation parameters from measured T_f data, we first simulated complete thermal histories along the surface, $T(r,t)$, for each laser exposure, and applied them to Eq.(9)-(11) to construct fitting functions for $T_f(r)$. A Levenberg-Marquardt algorithm was used to minimize χ^2 with no additional weighting. T_R was chosen to be 1453 K (published value of the annealing point for Homosil 102) while $\Delta H/R$ was fixed at 65,200 K based on viscosity measurements of type II glass (Weiss, 1984). Thus, x and τ_{ref} we allowed to vary, resulting in the average fit values presented in Table I. The results of the fitting method are shown in Fig. 7 (blue curves) demonstrating excellent agreement with the Raman data.

These derived relaxation parameters in the Tool- Naranaswamy model were found to be within the ranges found in the literature for type II silica based on differential thermal analysis (Bruning, 2003). The adjusted volume relaxation time pre-exponential parameter $\tau_{V\infty}$ is ~ 10 times that determined for the shear relaxation which in agreement with results obtained for other silicate glasses (Scherer, 1990). We also compared recent volume relaxation measurements (Sen et al., 2004) of $\tau_V(T)$ to our measured T_f data by again calculating $T_f(r)$ based on $T(r,t)$ and Eqs. (9)-(11) with x=1 (consistent with the observed Arrhenius behavior in that work). The result is shown as a red curve in Fig. 6, and also displays good agreement with our data. Interestingly, in both the fitted Tool-Narayanaswamy result and that based on (Sen et al., 2004) volume relaxation studies, , implying that silica relaxation, unlike other silica glasses, has little dependence on the fictive temperature, T_f. and is in agreement with recent results reported by (Tomozawa et al., 2008). The relative agreement with the fitted and calculated curves in Fig. 7 also demonstrates some degree of $\tau_V(T)$ model insensitivity to $\Delta H/R$ with varying τ_{ref} as in the latter case $\Delta H/R$ = 50,520 K (τ_{ref} =195 s) did not agree with the value of 65,200 K based on viscosity measurements of (Weiss, 1984).

With both T and T_f models validated, we can now explore the behavior of the laser-induced, temperature-dependent relaxation in more detail. As shown by the black curve in Fig. 8, the fictive temperature of silica retains the value of its annealed state until it is heated above the glass transition point, after which the fictive temperature begins to evolve as it tracks the thermodynamic temperature. Upon examining Fig. 7, it becomes apparent that the glass at radii larger than ~0.10 mm remained below the glass transition as its fictive temperature did not evolve. This is further corroborated upon examination of the temperature profiles in Fig. 6.

From Figs. 4 and 5, for radii between 0.07 and 0.13 mm, the thermodynamic temperature slightly exceeded the glass transition temperature, and the fictive temperature tracked the thermodynamic temperature. Once the laser shuts off, the glass in this vicinity cooled almost instantaneously to below the glass transition temperature. Due to the exceedingly high rate at which the thermodynamic temperature dropped below the glass transition temperature, the fictive temperature could not evolve rapidly enough to track the thermodynamic temperature, causing a new, larger than annealed state fictive temperature to be retained within the glass. This is depicted by the black curve in the left figure of Fig. 7, where the fictive

temperature does not evolve until the glass transition temperature is reached (t~180 ms), after which the fictive temperature and thermodynamic temperature track one another. Once the laser shut off, a slightly larger fictive temperature was frozen into the silica.

Again referring to Figs. 4 and 5, for radii less than 0.07 mm, the thermodynamic temperature greatly exceeded the glass transition temperature, causing the silica in this region to enter a temperature range where the structural relaxation of silica occurs rapidly. Once the laser shut off, cooling occurred at an extremely high rate, ~10^6 K/s. However, because of the high temperature in this region and associated short relaxation times (τ_V~10 μs), the fictive temperature was still able to track the cooling thermodynamic temperature. Due to the cooling and solidification of the silica, a lag developed between the thermodynamic temperature and the fictive temperature state and the two temperatures no longer tracked one another, causing the fictive temperature to gradually freeze in at temperatures above its annealed fictive temperature value, but below the peak temperature obtained in this region. The fictive temperature evolution of silica less than 0.07 mm radial from the beam center is displayed pictorially in the right of Fig. 7. As shown in Fig. 6, this resulted in the large dome shaped profile in the fictive temperature.

C. Surface Profiles

Due to heat from the laser and atomic ring network changes, the heated material will attempt to thermally expand. Because the material is constrained by surrounding material at lower temperature, the material cannot uniformly expand, causing features such as bumps and pits to develop on the surface. While the amount of material heated by the laser affects the extent and magnitude of the surface features, it is the thermal expansion which is ultimately responsible for the surface profile.

The initial attempt at determining thermal expansion which could reproduce the surface profiles of our four experiments was obtained from (Shelby, 2004). Due to the difficulty in directly measuring the thermal expansion of liquid silica at high temperatures, the thermal expansion had to be inferred in the manner of previous works (Douglas and Isard, 1951; Shelby, 2004)from the room temperature density difference measurements from samples which had been quenched from high temperatures. The resulting curve in density difference versus fictive temperature space fit a straight line with a slope of 4.2 x 10^{-6} /K. With the aide of Eq. (13) and assuming a constant solid volumetric thermal expansion coefficient of $\alpha_s = 1.65x10^{-6}$/K yielded a volumetric liquid thermal expansion coefficient of $\alpha_l = -2.55x10^{-6}$/K. With these values used in the simulations, the resulting computational surface profiles under predicted the experimental pit depths, as shown in Fig. 9(a).

With the poor agreement between the experiment and simulation profiles, it was necessary to modify the thermal expansion. Many of the detailed used to modify the thermal expansion curves are given in the discussion of the equation of state in Section II.C.2. Briefly, (Bruckner, 1970; Kuhn and Schadrack, 2009) show $\alpha(T)$ curves which indicate that the solid thermal expansion coefficient depends on fictive temperature. As it would have been difficult to incorporate a fictive temperature dependent thermal expansion into the Gibbs free-energy function of Eq. (7), a solid thermal expansion coefficient which averaged the influence of fictive temperature in the overall solid expansion coefficient was used in the simulations. This mean solid thermal expansion curve is the one listed in Table 1. With the absence of measured data for the liquid expansion curve, the liquid expansion was inferred by attempting to fit the experimental surface profiles shown in Fig. 9 and were highly constrained to match the measure fictive

temperature distributions and surface profiles of the four experiments. The expression listed in Table I is the results of this fitting process. Although we are not attempting to attribute any physical insight to the liquid curve obtained from this fitting process, it is interesting that the solid and liquid thermal expansion curves intersect around 2000 K, which is the melting temperature for silica. Although the simulation results do not exactly match the experiments, the results are close enough that the stresses which resulted from the material motion which produced these pits can now be examined. Before examining the stresses, it should be noted that it is the complex interaction of stress relaxation and structural relaxation which determined whether the resulting profile is a bump or a pit. Stress relaxation is responsible for creating a protrusion while structural or volume relaxation causes densification which leads to a depression.

D. Residual Stresses

Due to the non-uniform, rapid heating and cooling of the silica, residual stresses develop within the solid. In addition to the stresses which arise due to the viscous flowing and quenching of the material (stress relaxation), stress also develops due to frozen in fictive temperature states (structural relaxation). The structural relaxation stresses occur due to the material locking in at a particular material state set by the fictive temperature while the material really wants to evolve to the state dictated by the thermodynamic temperature. Stresses then develop as the material attempts to evolve to the thermodynamic temperature state but is prevented from reaching this state due to the slow evolution of its material properties.

Figure 10 contains stress contours for the heating and cooling of the silica by a 1.95 W (T_{max}=2031 K) laser exposure. The top row contains the maximum principle stress and shear stress as the laser turns off while the bottom row displays these stresses after the sample has returned to room temperature. In the top row, due to thermal expansion, the bulk of the material swelled, creating a bump. As the material at the center of the bump became hot enough for the fictive temperature to evolve, structural relaxation occurred in a narrow region near the surface. In this region, the material behaved as though it were a liquid and followed the liquid thermal expansion curve of Table I, resulting in the material contracting and forming a small pit. Because the material in this vicinity has been heated about the glass transition point, it behaves similar to a fluid and is able to flow, relaxing any thermal stresses which may have developed in the melted pool region. At the interface between the liquid-like and solid-like silica, a slightly stressed region develops as the material wants to flow, but is not hot enough to completely relax.

Upon cooling, the stresses shown in the lower row of Fig. 10 are permanently set into the glass. As the material which formed the bump remained below the glass transition temperature, the thermal expansion of this material was completely recoverable. In the material where the temperature exceeded the glass transition temperature, material flowed and the SiO_2 ring network evolved into a configuration of a higher temperature network. This high temperature configuration was then locked into the glass due to the high cooling rates in the silica. Due to the thermal contraction in the liquid, a permanent pit formed at the surface.

Residual tensile stresses develop along the surface of the pit once it has returned to room temperature. As a pit was formed, it may be anticipated that stresses along the surface should be compressive. However, due to the interaction of solid-like and liquid-like material regions, as well as the rapid cooling rate, surface tensile stresses do develop. Almost as soon as the laser turns off, the liquid material freezes into its current configuration with the pit. As cooling progresses, the solid material region which had thermal expanded to form the bump now begins to contract back to its initially position as no irrecoverable material state changes have occurred. When the solid material has hot, it expanded both upward against the surface as well as inward, attempting to close the pit. With the material returned to room temperature, the bump attempts to once again become a flat surface, contracting the surface and

pulling on the pit. It is this pulling on the once again solidified pitted surface which creates tensile surface stresses. As the material is not able to fully return to it initial position due to the pit, compressive stresses develop below the pit, just outside the region which had transitioned above the glass transition temperature.

In a recent study, a method was developed to mitigate optical damage on type III fused silica surfaces using localized CO_2 laser heating (Adams et al., 2010; Matthews et al., 2009). Fractured surfaces created during laser-induced breakdown were subsequently annealed using this method, with peak temperatures near 2000 K and hold times on the order of several seconds. On this time and temperature scale, the silica glass is expected to contain stress fields similar to those shown in Fig. 10. The magnitude of the tensile stresses becomes important when considering subsequent damage initiation and crack growth along the portion of silica surface which has been laser-heated. Fig. 11a shows an image of an optical damage site created within a CO_2 laser heated region, as described in Matthews et al., 2009. Also shown in Fig. 11a is a lineout of the principal stresses when decomposed into its hoop and radial components. In creating the stress curves in the left of Fig. 10, lineouts were sent through the thickness of the sample and the maximum tensile stress found along the lineout was recorded. The radial location was then increased and another lineout operation was performed. The depth at which the maximum tensile stress occurred was also monitored, and they were found to lie near the surface.

That the maximum tensile stress is found at the surface is important, as any surface crack which starts to grow will continue to grow until it exits the high tensile stress field, resulting in large cracks causing extensive damage. Within some damage site dimension limit however, the associated flaw sizes will be too small to support crack propagation under a given finite stress field (Lawn, 1993). However, when the flaw length exceeds a critical limit, a crack can propagate from the damage causing catastrophic failure. By gradually increasing the initiated damage site dimension in a fixed residual stress field, an experimental estimate of the critical stress was estimated to be 29±3.1 MPa, in good agreement with a calculated maximum hoop stress of ~25 MPa. Morphologically, the black line extending from the damaged area in Fig. 11a is a crack which propagated through the high stressed region. Notably, it eventually turned radial and halted where the hoop stress, which drove the crack growth, rapidly dropped below the radial stress.

Measurements of the stress optic coefficient were also performed for a more quantitative estimate of how well the computational model predicts stresses. Stresses in silica affect the refractive indices of the material, which leads to phase retardation of light as it passes through the silica. The more highly stressed the glass, the greater the retardation. By plotting the transmission intensity obtained experimentally from polarimetry against the integrated peak stress difference along *r*, , a stress optic coefficient C~33 nm/cm/MPa was obtained through least-squares fitting, as shown by the red curve of Fig. 11b. The fitted curve agrees quite well with that based on the accepted theoretical value for the stress optic coefficient of silica, C=35.5 nm/cm/MPa, indicating that the computed stresses are of the correct magnitude. A benefit of the code is that experimentally, only the integrated stress difference values can be obtained while the code allows the individual components comprising the stress difference to also be determined.

As a considerable amount of time was spent developing and coupling the structural relaxation model to the other physics models as well as obtaining experimental measurements of the fictive temperature, it is desirable to examine the influence of structural relaxation. Fig. 10(a) contains the hoop and radial stress for two almost identical simulations, the only difference being that in one simulation structural relaxation was allowed to occur while in the other, structural relaxation was turned off. The resulting stress lineouts shown in Fig. 10(a) indicate that structural relaxation has little effect on the stress magnitude and location. Based on the stresses alone, it would appear structural relaxation is of negligible importance. However, as structural relaxation describes the local ring structure configuration of the silica, it effects more material states than just the stress. This becomes apparent upon examining the density

contours in Fig. 20, where the figure on the left includes structural relaxation while the one on the right does not.

Substantial differences are now detectable in the region where the thermodynamic temperature exceeded the initial annealed fictive temperature value. In the left half of Fig. 12, the high temperature region behaves liquid-like, structural relaxation allowed the material to volumetrically contract, leading to an increase in density and a permanent pit to form in the surface. In the right half of Fig. 12, the heated liquid region was not allowed to structural relax. Without any volumetric contraction, upon cooling the material froze in at its expanded state, resulting in a slightly lower density material at the surface, but more importantly, a permanent bump formed in place of the pit. By ignoring structural relaxation, not only does the surface profile change from concave to convex, but now instead of acting as a light intensifier which can produce further damage in the glass, the silica surface becomes a diffuser which helps to disperse and defocus laser light.

V. Conclusion

The effect of depositing laser energy near the surface of a silica sample have been examined in terms of the resulting thermal profile which then produced changes in the Si-O bonding arrangements within the glassy network and resulted in deformation of the material and residual stresses Unlike a recent thermomechanical study of aluminosilicate glass heated by a CO_2 laser (Bennett and Li, 2001) no plastic flow was assumed but both stress and structural relaxation were included. Thermal calculations carefully derived from existing and extrapolated material models were validated using deconvolved in situ pyrometry. Good agreement with experimental measurements of the transient surface temperature profile was found. Confocal Raman scattering of the Si-O asymmetric stretch mode was used to spatially-resolve fictive temperature variations, and, with the predicted temperature-time histories as inputs led to derivation of structural relaxation parameters. Both least squares fits and predictions based on Sen et al., 2004 yielded excellent agreement with fictive temperature data. Surface depressions caused by the laser heating were measured using white light interferometry, and could be compared to predictions using our model and expressions for volumetric thermal expansion. It was found that structural deformations predicted using density measurements of Shelby and/or Bruckner et al. 1970 underestimated the final surface depressions, while a ~2x steeper liquid expansion reasonably agreed with our measured data. Notably, only when both stress and structural relaxation are taken into account can the observed surface profile be understood. Our modeling allowed a glimpse at high temperature volumetric changes which are difficult to study due to very short relaxation times, yielding rough estimates to silica liquid thermal expansion values. Finally, integrated stress differential calculations were used with birefringence measurements to estimate the stress optic coefficient of silica (C~32.8 nm/cm/MPa), while surface tensile stress predictions could be compared with previously-published critical fracture experiments, yielding good agreement.

Appendix: Material response based on Equation of State modeling

For this study, a thermodynamically consistent equation of state has been developed. The development of this model is founded on the premise that one can relate the isothermal bulk modulus (K_T), specific heat (C_P), and coefficient of thermal expansion (α) to the Gibbs Free Energy (G) through standard thermodynamic relations. These relations, with their assumed linearly-expanded temperature and pressure variance from a reference point on the state diagram (T_0, P_0) are expressed as:

$$
\begin{aligned}
-\left(\frac{\partial G}{\partial V}\right)_T &= K_T = k_0 + k_P (P - P_0) + k_T (T - T_0) + k_{PT} (T - T_0)(P - P_0), \\
-T\left(\frac{\partial^2 G}{\partial T^2}\right)_P &= C_P = c_0 + c_T (T - T_0), \\
\frac{1}{V}\left(\frac{\partial^2 G}{\partial P \partial T}\right)_{PT} &= \alpha = \alpha_0 + \alpha_T (T - T_0).
\end{aligned}
\tag{A1}
$$

To adequately represent a material with parameters that vary with temperature in a non-linear fashion, the relations in equations (A1) are applied to multiple temperature ranges to describe K_T, C_P and α over a wide range of temperatures. By integrating the three expressions in Eq. (A1) and combining them, we postulate an expression for Gibbs free energy:

$$
\begin{aligned}
G(P,T) = G_0 &+ \left(c_0 - S_0 - \frac{1}{2} c_T (T + T_0)\right)(T - T_0) - T\,(c_0 - c_T T_0) Log\left(\frac{T}{T_0}\right), \\
&+ \left(\left(\frac{k_0 + k_T (T - T_0)}{K_T (P,T)}\right)^{\frac{1}{K_p} - 1} - 1\right) \frac{(k_0 + k_T (T - T_0))}{K_p - 1} V_1
\end{aligned}
\tag{A2}
$$

where :

$$K_p = k_P + k_{PT} (T - T_0), \text{and}$$

$$V_1 = e^{(\alpha_0 + \frac{1}{2}\alpha_t (T - T_0))(T - T_0)} V_o,$$

Note that in Eq. (A2), when K_p is equal to zero or unity, then the expression for last term of Eq. (A2) contains a singularity. However the limits exist and a series expansion of Eq. (A2) is used when those situations arise. The entropy (S) of the material is then expressed as:

$$
\begin{aligned}
S(P,T) = S_0 &+ c_t\,(T - T_o) + (c_o - c_t\,T_o)\,Log\left(\frac{T}{T_o}\right) + K_t\, h^{K_p}\, V\, \alpha \\
&+ \left[\frac{h^{Kp} - 1}{K_p}\left(k_t + \frac{K_t k_{pt}}{K_p}\right) + \frac{h^{K_p} Log(h)}{K_p}\right] V \\
&+ \left[\frac{1 - h^{Kp}}{K_p - 1}\left(k_t - K_t\left(\frac{k_{pt}}{K_p - 1} - \alpha K_p\right)\right) - \frac{h^{Kp} k_{pt} Log[h]}{K_p - 1}\right] V_1,
\end{aligned}
\tag{A3}
$$

where :

$$h = \frac{V_1}{V}.$$

As was the case with the expression for G, the expression for S also contains a singularity when $K_p=1$, in which case series expansion of Eq. (A3) are used in place. Taking the derivative of G with respect to

pressure (P) yields an expression for volume (V). This expression for V is inverted to yield and expression for pressure:

$$V(P,T) = \frac{\partial G}{\partial P} = \left(\frac{k_0 + k_T(T - T_0)}{K_T(P,T)} \right)^{\frac{1}{k_P + k_{PT}(T - T_0)}} V_0 e^{\left(\alpha_0 + \frac{1}{2}\alpha_T (T - T_0)\right)(T - T_0)}$$

$$P(V,T) = P_0 + \frac{k_0 + k_T(T - T_0)}{k_P + k_{PT}(T - T_0)} \left(\left(\frac{V_0 e^{\left(\alpha_0 + \frac{1}{2}\alpha_T (T - T_0)\right)(T - T_0)}}{V} \right)^{k_P + k_{PT}(T - T_0)} - 1 \right) \qquad \text{(A4)}$$

With Eqs. (A2, A3, A4) we are able to calculate the internal energy (U) of the material using the relationship:

$$U(V,T) = G(P,T) + S(P,T)T - P(V,T)V. \qquad \text{(A5)}$$

In the context of the finite element method utilized in this study, the independent variables passed into the material routines are volume (V) and internal energy (U). Thus we must use a simple Newton iterative scheme to solve for the temperature (T) that yields the specified internal energy (U).

The application of the fictive temperature (T_f) to this equation of state is accomplished by dividing the relative volume (V) that is input into (A4) by a modification factor (V_f). The evolution of (V_f) from time (t^n) to time (t^{n+1}) is defined by:

$$V_f^{n+1} = V_f^n \frac{1 + \frac{1}{2}\left[\alpha_l(T_f^{n+\frac{1}{2}}) - \alpha_s(T_f^{n+\frac{1}{2}})\right]\Delta T_f}{1 - \frac{1}{2}\left[\alpha_l(T_f^{n+\frac{1}{2}}) - \alpha_s(T_f^{n+\frac{1}{2}})\right]\Delta T_f},$$

where :

$$\Delta T_f = T_f^{n+1} - T_f^n, \qquad \text{(A5)}$$

$\alpha_l, \alpha_s =$ liquid and solid coefficien t of thermal expansion.

References

Adams, J.J., Bolourchi, M., Bude, J.D., Guss, G.M., Matthews, M.J., Nostrand, M.C., 2010. Results of applying a non-evaporative mitigation technique to laser-initiated surface damage on fused-silica, in: Exarhos, G.J.G.V.E.M.J.A.R.D.S.M.J. (Ed.), Laser-Induced Damage in Optical Materials: 2010.

Agarwal, A., Davis, K.M., Tomozawa, M., 1995. A Simple Ir Spectroscopic Method for Determining Fictive Temperature of Silica Glasses. Journal of Non-Crystalline Solids 185, 191-198.

Angell, C.A., Kanno, H., 1976. Density Maxima in High-Pressure Supercooled Water and Liquid Silicon Dioxide. Science 193, 1121-1122.

Anthony, T.R., Cline, H.E., 1977. Surface Rippling Induced by Surface-Tension Gradients during Laser Surface Melting and Alloying. J Appl Phys 48, 3888-3894.

Armero, F., Simo, J.C., 1992. A new unconditionally stable fractional step method for nonlinear coupled thermomechanical problems. Int. J. Numer. Methods Eng. 35, 737-766.
Armero, F., Simo, J.C., 1993. A priori stability estimated and unconditionally stable product formula algorithms for nonlinear coupled thermoplasticity. Int. J. Plast. 9, 749-782.
Barborica, A., Mihailescu, I.N., Teodorescu, V.S., 1994. Dynamical Evolution of the Surface Microrelief under Multiple-Pulse-Laser Irradiation - an Analysis Based on Surface-Scattered Waves. Phys Rev B 49, 8385-8395.
Bass, I.L., Guss, G.M., Nostrand, M.J., Wegner, P.J., 2010. An Improved Method of Mitigating Laser Induced Surface Damage Growth in Fused Silica Using a Rastered, Pulsed CO(2) Laser, in: Exarhos, G.J., Gruzdev, V.E., Menapace, J.A., Ristau, D., Soileau, M.J. (Eds.), P Soc Photo-Opt Ins.
Bennett, T.D., Krajnovich, D.J., Li, L., 1999. Thermophysical modeling of bump formation during CO2 laser texturing of silicate glasses. Journal of Applied Physics 85, 153-159.
Bennett, T.D., Krajnovich, D.J., Li, L., Wan, D.J., 1998. Mechanism of topography formation during CO2 laser texturing of silicate glasses. J. Appl. Phys. 84, 2897-2905.
Bennett, T.D., Li, L., 2001. Modeling laser texturing of silicate glass. J. Appl. Phys. 89, 942-950.
Bouchut, P., Delrive, L., Decruppe, D., Garrec, P., 2004. Local re-fusion of silica, by a continuous CO2 laser, for the mitigation of laser damage growth. Optical Fabrication, Testing, and Metrology 5252, 122-130.
Bruckner, R., 1970. Properties and Structure of Vitreous Silica I. J Non-Cryst Solids 5, 123-175.
Bruning, R., 2003. On the glass transition in vitreous silica by differential thermal analysis measurements. J Non-Cryst Solids 330, 13-22.
Churchill, S.W., Chu, H.H.S., 1975. Correlating Equations for Laminar and Turbulent Free Convection from a Horizontal Cylinder. International Journal of Heat and Mass Transfer 18, 1049-1053.
Corning, Corning 7980 Datasheet.
Dahmani, F., Schmid, A.W., Lambropoulos, J.C., Burns, S., 1998. Dependence of birefringence and residual stress near laser-induced cracks in fused silica on laser fluence and on laser-pulse number. Applied Optics 37, 7772-7784.
Douglas, R.W., Isard, J.O., 1951. Density Changes in Fused Silica. J. Soc. Glass Technol. 35, 206-225.
Elhadj, S., Matthews, M.J., Yang, S.T., Cooke, D.J., Stolken, J.S., Vignes, R.M., Draggoo, V.G., Bisson, S.E., 2010. Determination of the intrinsic temperature dependent thermal conductivity from analysis of surface temperature of laser irradiated materials. Applied Physics Letters 96, 0171101-0171103.
Galeener, F.L., 1982. Planar Rings In Vitreous Silica. J Non-Cryst Solids 49, 53-62.
Geissberger, A.E., Galeener, F.L., 1983. Raman studies of vitreous SiO_2 versus fictive temperature. Phys. Rev. B 28, 3266-3271.
Han, L.J., Liou, F.W., Musti, S., 2005. Thermal behavior and geometry model of melt pool in laser material process. J. Heat Transf.-Trans. ASME 127, 1005-1014.
Hau, L.P., 2011. private communication.
Heraeus, Heraeus Quartzglass database.
Hilber, H.M., Hughes, T.J.R., Taylor, R.L., 1977. Improved numerical dissipation for time integration algorithms in structural dynamics. Earthq. Eng. Struct. Dyn. 5, 283-292.
Hnatovsky, C., Taylor, R.S., Simova, E., Rajeev, P.P., Rayner, D.M., Bhardwaj, V.R., Corkum, P.B., 2006. Fabrication of microchannels in glass using focused femtosecond laser radiation and selective chemical etching. Appl. Phys. A-Mater. Sci. Process. 84, 47-61.
Horstmann-Jungemann, M., Gottmann, J., Wortmann, D., 2009. Nano- and Microstructuring of SiO(2) and Sapphire with Fs-laser Induced Selective Etching. J. Laser Micro Nanoeng. 4, 135-140.
Kakiuchida, H., Saito, K., Ikushima, A.J., 2003. Precise determination of fictive temperature of silica glass by infrared absorption spectrum. J. Appl. Phys. 93, 777-779.
Kaplan, A.F.H., Tokarev, V.N., 1999. An analytical modeling of time dependent pulsed laser melting. J. Appl. Phys. 86, 2836-2846.

Kim, D.Y., Li, L., Jiang, X.L., Shivshankar, V., Kumar, J., Tripathy, S.K., 1995. Polarized laser induced holographic surface relief gratings on polymer films. Macromolecules 28, 8835-8839.
Kingery, W.D., 1961. Heat-Conductivity Processes in Glass. J Am Ceram Soc 44, 302-304.
Kitamura, N., Fukumi, K., Nishii, J., Kinoshita, T., Ohno, N., 2003. Formation of microdots on the surface of densified silica glass by thermal relaxation. Jpn J Appl Phys 2 42, L712-L714.
Koshiba, K., Honma, T., Benino, Y., Komatsu, T., 2007. Patterning and morphology of nonlinear optical GdxBi1-xBO3 crystals in CuO-doped glass by YAG laser irradiation. Applied Physics a-Materials Science & Processing 89, 981-986.
Kuhn, B., Schadrack, R., 2009. Thermal expansion of synthetic fused silica as a function of OH content and fictive temperature. J Non-Cryst Solids 355, 323-326.
Lawn, B., 1993. Fracture of Brittle Solids - Second Edition. Cambridge University Press, New York.
Lax, M., 1977. Temperature Rise Induced by a Laser-Beam. J. Appl. Phys. 48, 3919-3924.
Lax, M., 1978. Temperature Rise Induced by a Laser-Beam .2. Non-Linear Case. Applied Physics Letters 33, 786-788.
Mann, D., Field, R.E., Viskanta, R., 1992. Determination of Specific-Heat and True Thermal-Conductivity of Glass from Dynamic Temperature Data. Warme Stoffubertrag 27, 225-231.
Markovsky, A., Soules, T.F., 1984. An Efficient and Stable Algorithm for Calculating Fictive Temperatures. Journal of the American Ceramic Society 67, C56-C57.
Matthews, M.J., Stolken, J.S., Vignes, R.M., Norton, M.A., Yang, S., Cooke, J.D., Guss, G.M., Adams, J.J., 2009. Residual stress and damage-induced critical fracture on CO 2 laser treated fused silica. Proceedings of the SPIE - The International Society for Optical Engineering 7504.
Matthews, M.J., Vignes, R.M., Cooke, D., Yang, S.T., Stolken, J.S., 2010. Analysis of micro-structural relaxation phenomena in laser-modified fused silica using confocal Raman microscopy. Opt Lett 35, 1-3.
McLachlan, A.D., Meyer, F.P., 1987. Temperature dependence of the extinction coefficient of fused-silica for CO_2-laser wavelengths. Applied Optics 26, 1728-1731.
McMillan, P.F., Poe, B.T., Gillet, P., Reynard, B., 1994. A STUDY OF SIO2 GLASS AND SUPERCOOLED LIQUID TO 1950 K VIA HIGH-TEMPERATURE RAMAN-SPECTROSCOPY. Geochim. Cosmochim. Acta 58, 3653-3664.
Mendez, E., Nowak, K.M., Baker, H.J., Villarreal, F.J., Hall, D.R., 2006. Localized CO2 laser damage repair of fused silica optics. Applied Optics 45, 5358-5367.
Narayanaswamy, O.S., 1971. Model of Structural Relaxation in Glass. J Am Ceram Soc 54, 491-&.
Philipp, H.R., 1985. in: Palik, E.D. (Ed.), Handbook of Optical Constant of Solids. Academic, New York, p. 762.
Polian, A., Vo-Thanh, D., Richet, P., 2002. Elastic properties of a-SiO2 up to 2300 K from Brillouin scattering measurements. Europhysics Letters 57, 375-381.
Rozenbaum, O., Meneses, D.D., Auger, Y., Chermanne, S., Echegut, P., 1999. A spectroscopic method to measure the spectral emissivity of semi-transparent materials up to high temperature. Rev. Sci. Instrum. 70, 4020-4025.
Rubenchik, A.M., Feit, M.D., 2003. Mechanisms of CO2 laser mitigation of laser damage growth in fused silica, Laser-Induced Damage in Optical Matls. 2002/7th Intl. Wkshp. on Laser Beam & Optics Characterization. SPIE.
Ryu, S.R., Tomozawa, M., 2006. Fictive temperature measurement of amorphous SiO2 films by IR method. Journal of Non-Crystalline Solids 352, 3929-3935.
Scherer, G.W., 1986. Volume Relaxation Far from Equilibrium. J Am Ceram Soc 69, 374-381.
Scherer, G.W., 1990. Theories of Relaxation. J Non-Cryst Solids 123, 75-89.
Scherer, G.W., 1993. Structural Relaxation. Plastics Rubber and Composites Processing and Applications 19, 1-5.
Sen, S., Andrus, R.L., Baker, D.E., Murtagh, M.T., 2004. Observation of an anomalous density minimum in vitreous silica. Physical Review Letters 93.
Shelby, J.E., 2004. Density of vitreous silica. J Non-Cryst Solids 349, 331-336.

Shen, N., Matthews, M.J., Fair, J.E., Britten, J.A., Nguyen, H.T., Cooke, D., Elhadj, S., Yang, S.T., 2010. Laser smoothing of sub-micron grooves in hydroxyl-rich fused silica. Appl Surf Sci 256, 4031-4037.
Shestakov, A.I., Vignes, R.M., Stolken, J.S., 2011. Derivation and solution of multifrequency radiation diffusion equations for homogeneous refractive lossy media. J. Comput. Phys. 230, 984-999.
Sorescu, M., Knobbe, E.T., 1994. INDUCED ANISOTROPY AND PHASE-TRANSFORMATION IN METALLIC GLASSES BY PULSED-EXCIMER-LASER IRRADIATION. Physical Review B 49, 3253-3265.
Soules, T.F., Busbey, R.F., Rekhson, S.M., Markovsky, A., Burke, M.A., 1987. Finite-Element Calculation of Stresses in Glass Parts Undergoing Viscous Relaxation. Journal of the American Ceramic Society 70, 90-95.
Tomozawa, M., Koike, A., Ryu, S.R., 2008. Exponential structural relaxation of a high purity silica glass. J Non-Cryst Solids 354, 4685-4690.
Tool, A.Q., 1945. Relaxation of Stresses in Annealing Glass. J Res Nat Bur Stand 34, 199-211.
Tool, A.Q., 1946. Relation between Inelastic Deformability and Thermal Expansion of Glass in Its Annealing Range. Journal of the American Ceramic Society 29, 240-253.
Veiko, V.P., Kieu, Q.K., Nikonorov, N.V., Shur, V.Y., Luches, A., Rho, S., 2005. Laser-induced modification of glass-ceramics microstructure and applications. Appl Surf Sci 248, 231-237.
von Allmen, M., Blatter, A., 1998. Laser-Beam Interactions with Materials, second ed. Springer-Verlag, Hiedelberg.
Wakaki, M., Komachi, Y., Kanai, G., 1998. Microlenses and microlens arrays formed on a glass plate by use of a CO2 laser. Appl Optics 37, 627-631.
Weiss, W., 1984. A Rapid Torsion Method for Measuring the Viscosity of Silica Glasses up to 2200-Degrees-C. J Am Ceram Soc 67, 213-222.
Wray, K.L., Connolly, T.J., 1959. Thermal Conductivity of Clear Fused Silica at High Temperatures. J. Appl. Phys. 30, 1702-1705.
Yanenko, N.N., 1971. The Method of Fractional Steps. Springer-Verlag, New York.
Yang, S.T., Matthews, M.J., Elhadj, S., Draggoo, V.G., Bisson, S.E., 2009. Thermal transport in CO_2 laser irradiated fused silica: In situ measurements and analysis. J. Appl. Phys. 106, 1031061-1031067.
Zhao, J., Sullivan, J., Zayac, J., Bennett, T.D., 2004. Structural modification of silica glass by laser scanning. Journal of Applied Physics 95, 5475-5482.

Prepared by LLNL under Contract DE-AC52-07NA27344.

Table I: Silica thermal and relaxation parameters used in the calculations

Property	Symbol	Value	Units
Shear modulus	G	31.3	GPa
Density at $T=298K$	ρ_0	2.201	g/cm^3
Solid volume thermal expansion coefficient	α_s	$2.91\times10^{-6} - 1.47\times10^{-9} \times T(K)$	
Liquid volume thermal expansion coefficient	α_l	$-49.93\times10^{-6} + 27.52\times10^{-9} \times T(K)$	
Fictive temperature at t=0 (measured from IR)	T_f(t=0)	1431	K
Reference temperature for relaxation time	T_R	1453	K
Shear relaxation time at $T=\infty$ from η/G	$\tau_{S\infty}$	1.039×10^{-18}	s
Structural relaxation time at $T=\infty$ from fit	$\tau_{V\infty}$	1.064×10^{-17}	s
Enthalpy for shear stress and structural relaxation (from Homosil - T_{anneal}=1180 C and T_{soften}=1730 C)	$\Delta H/R$	65,200	K
Parameter to divide enthalpy between T and T_f from fit	x	0.9	

Table II: Laser parameters and measured peak T, T_f values.

Sample	OH content (%w ppm)	P (W)	d (μm)	t_exp (s)	T_{max} (K)	$T_{f,\,max}$ (K)
H102-A	150	1.65	390	5	1839±55	1760±34
H102-A	150	1.75	390	5	1892±57	1848±30
H102-A	150	1.85	390	5	1989±60	1922±30
H102-A	150	1.95	390	5	2031±61	1993±36
C7980	~500	12	2000	40	~2300	~1900

Figure captions:

Figure 1: Thermal expansion and contraction of liquid silica as measured by Sen et al., 2004 at low temperatures and constructed by Bruckner et al., 1970 for higher temperatures. The data are referenced to values at 1450 K. Also shown are sketches suggesting possible structures for the low and high density amorphous phases in the liquid. Kuhn's data is shown for the metastable solid silica glass.

Figure 2: (a) Heat capacity C_P (dashed) and thermal conductivity κ (solid) as a function of temperature for silica determined as described in the the text and used in the calculations. (b) Directionally-averaged sound velocity v after (Polian et al., 2002) (dashed) and derived phonon mean free path Λ as a function of temperature.

Figure 3: Influence of the various heat loss cooling boundary conditions estimated for steady-state, 10.6 μm laser heating of silica.

Figure 4: Bulk moduli components for the equation of state model. Fig. (a) contains the temperature and pressure dependent contributions to the total bulk modulus while Fig. (b) depicts the isothermal bulk modulus.

Figure 5: Schematic of optical system and MCT camera used for in-situ surface temperature measurement of CO_2 laser heated samples. The red solid line marks the CO_2 laser beam path; the blue dotted line indicates the emitted thermal emission. Cf1, Cf2, f1 and f2 are ZnSe lenses; TEL1 is a telescope with variable magnification; BP is the narrow-band bandpass cold filter centered at 8.9 μm placed immediately in front of the MCT camera.

Figure 6: Temperature distributions for four laser powers. The temperature profiles are measured after 5 seconds of heating with the laser just before the laser is turned off. As discussed in the text, the black circles are temperatures computed directly from pixel intensities measured at an angle. The red curves are calculated from the model.

Figure 7: Measured (open symbols) and calculated (lines) surface fictive temperatures T_f for four peak laser powers following thermal quench. The blue curves are fits to the measured data using Eqs. (9)-(11) in conjunction with calculated $T(r,t)$ along the surface while the red curves were calculated based on the volume relaxation measurements of (Sen et al., 2004).

Figure 8: Calculated fictive temperatures (black line and left axis) and free volume (red line and right vertical axis) during a simulated linear heating (1.85 W laser), a hold for 5 s and rapid cooling of one element. Far from the peak in incident laser power (a), peak surface temperatures reach ~1600 K and fictive temperatures are immediately frozen in during cooling. Near the center of the laser beam (b), temperatures approach 1900 K and exceed those required for relaxation over laser exposure time scales.

Figure 9: Measured and calculated surface profiles for the four laser-treated surfaces. Calculated curves are based on (a) a linear liquid thermal expansion curve derived from the density measurements of (Shelby, 2004) and (b) a piece-wise linear liquid expansion derived from our data. The experimental data has been azimuthally-averaged. The inset shows the net volume change for both model and experiment.

Figure 10: Snap shot of stress states at laser shut off (a,b) and after the silica sample has returned to room temperature (c,d). (a) and (c) contain the maximum principal stress while (b) and (d) contain the shear stress. A positive value for the principal stress indicates tension. The stresses in these plots were produced by heating the sample with the 1.95 W laser. In order to visualize the displacements and the stresses

together, in creating the images, the displacement field has been scaled by a factor of 500. In the figures then, a displacement of 0.25 mm is actually 500 nm.

Figure 11: (a) Observed crack propagation from an optical damage site initiated in a region densified from laser heating (P=12W, d=2mm, t=40s). The calculated hoop and radial stresses are also shown, indicating an upturn in the radial component near crack deflection for calculations including structural relaxation (solid curves) as compared to those without (dashed curves). (b) Stress induced birefringence measurements using polarimetry plotted against the integrated local stress difference ξ.

Figure 12: Final density contours superposed on the deformed surface profile, indicating the effect of structural relaxation. The profile in the left half of the figure includes a volume relaxation with an activation enthalpy of $\Delta H/R = 65{,}200$ as discussed in the text. In the right half of the figure the volume relaxation was turned off.

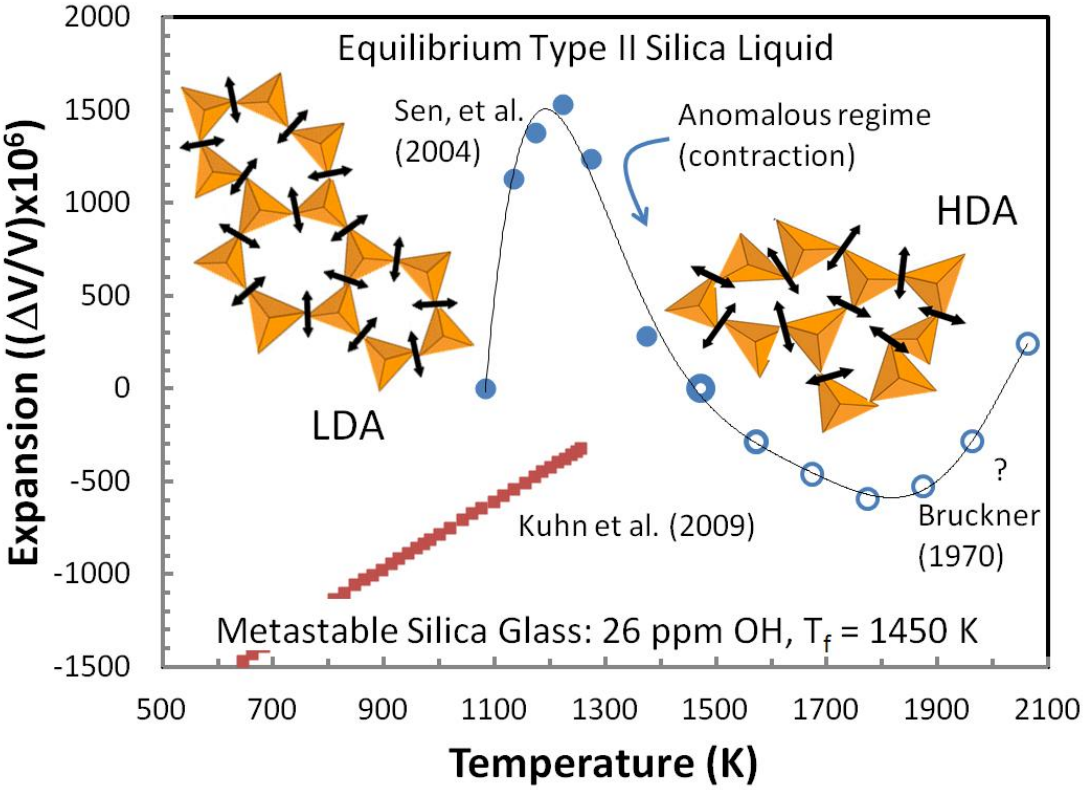
Equilibrium Type II Silica Liquid
Sen, et al. (2004)
Anomalous regime (contraction)
HDA
LDA
Kuhn et al. (2009)
?
Bruckner (1970)
Metastable Silica Glass: 26 ppm OH, T_f = 1450 K
Expansion ((ΔV/V)x10^6)
Temperature (K)
2000
1500
1000
500
0
-500
-1000
-1500
500
700
900
1100
1300
1500
1700
1900
2100

FIGURE 1

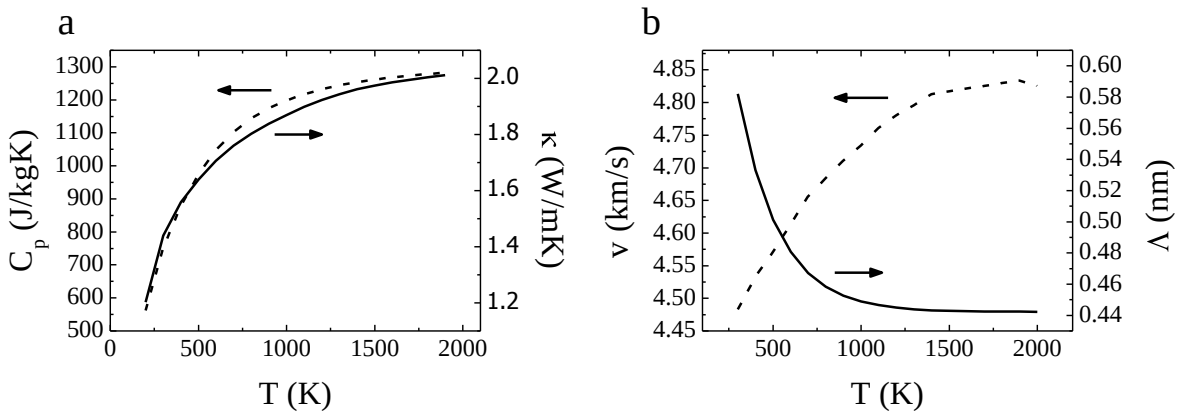
a
1300
1200
1100
1000
900
800
700
600
500
0
500
1000
1500
2000
T (K)
C_p (J/kgK)
2.0
1.8
1.6
1.4
1.2
κ (W/mK)
b
4.85
4.80
4.75
4.70
4.65
4.60
4.55
4.50
4.45
500
1000
1500
2000
T (K)
v (km/s)
0.60
0.58
0.56
0.54
0.52
0.50
0.48
0.46
0.44
Λ (nm)

FIGURE 2

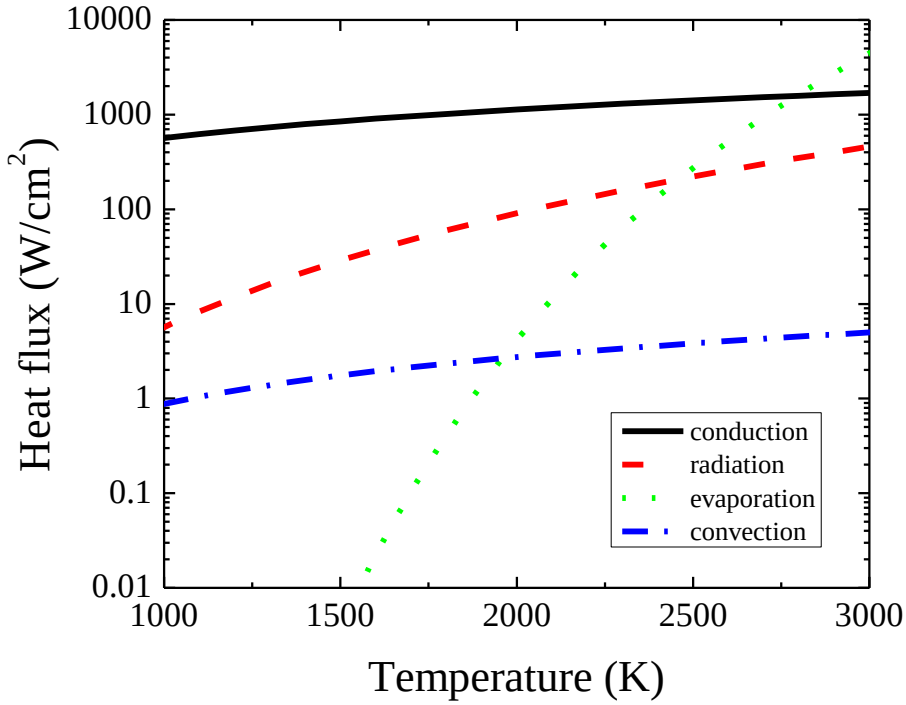
10000
1000
100
10
1
0.1
0.01
Heat flux (W/cm^2)
1000
1500
2000
2500
3000
Temperature (K)
conduction
radiation
evaporation
convection

FIGURE 3

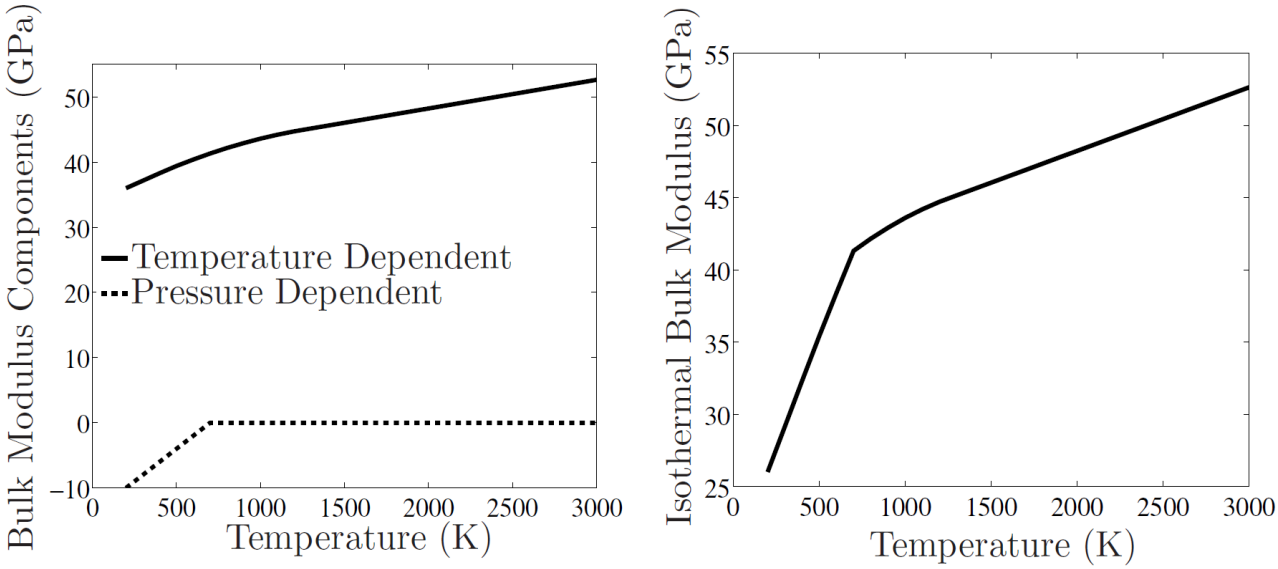
Bulk Modulus Components (GPa)
Temperature Dependent
Pressure Dependent
Temperature (K)
Isothermal Bulk Modulus (GPa)
Temperature (K)

FIGURE 4

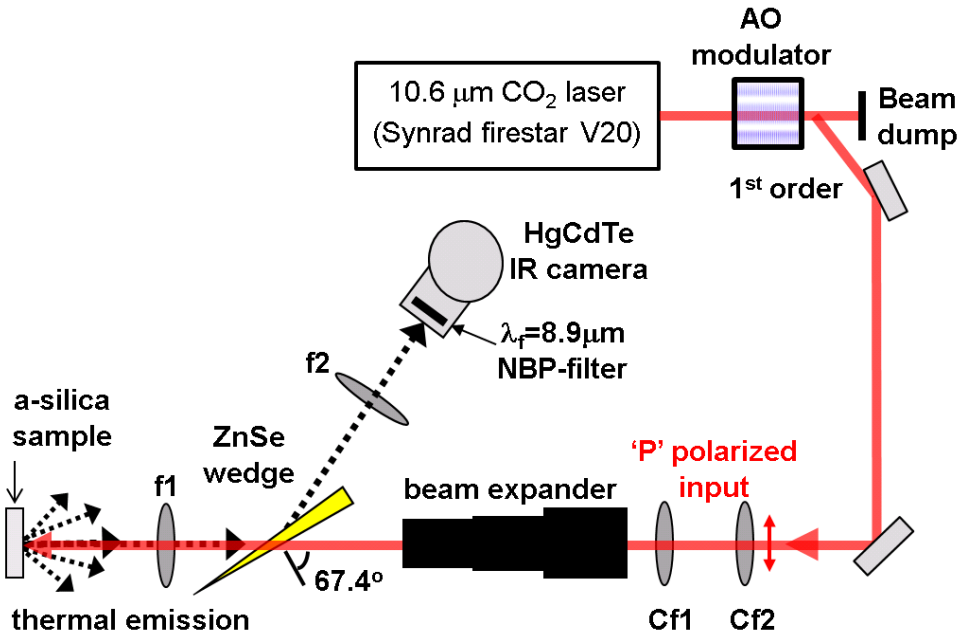
AO
modulator
10.6 μm CO_2 laser
(Synrad firestar V20)
Beam
dump
1st order
HgCdTe
IR camera
λ_f=8.9μm
NBP-filter
f2
a-silica
sample
ZnSe
wedge
f1
beam expander
'P' polarized
input
67.4°
thermal emission
Cf1
Cf2

FIGURE 5

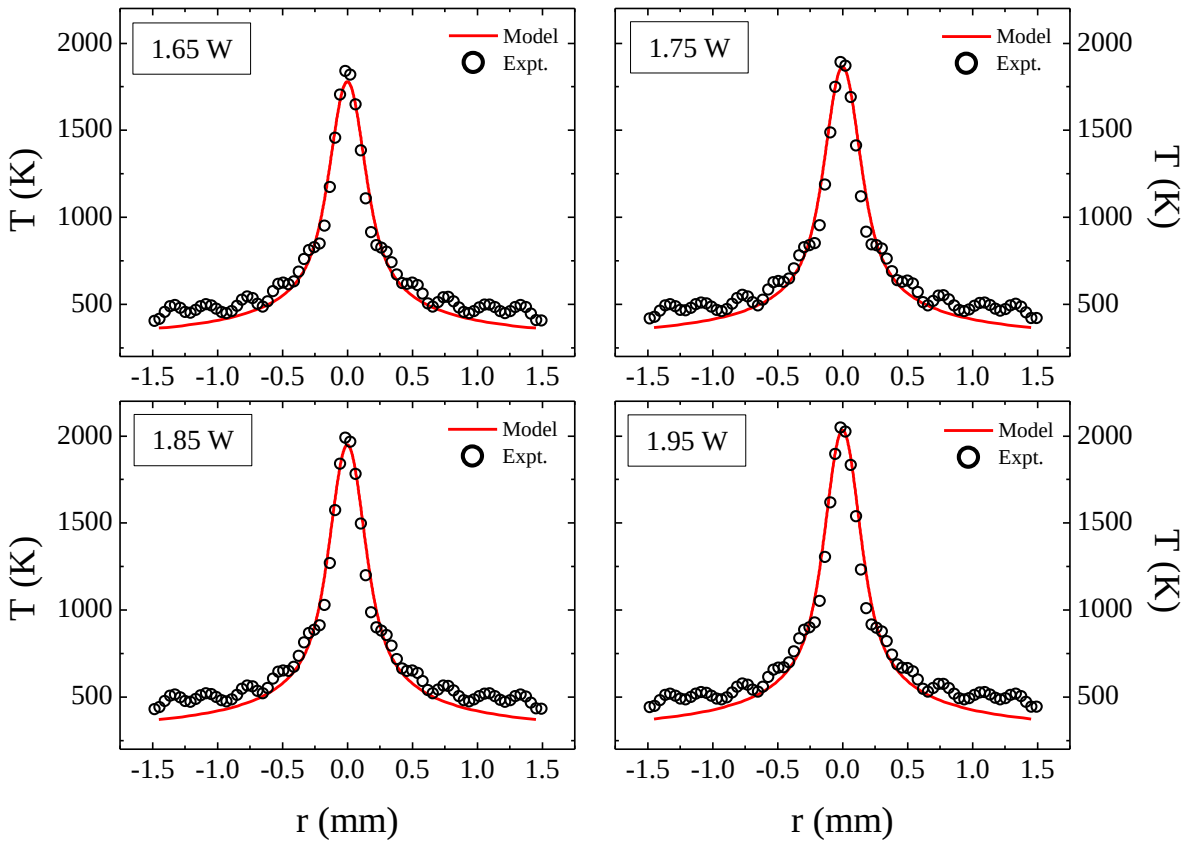
1.65 W
1.75 W
1.85 W
1.95 W
Model
Expt.
T (K)
r (mm)
2000
1500
1000
500
-1.5
-1.0
-0.5
0.0
0.5
1.0
1.5

FIGURE 6

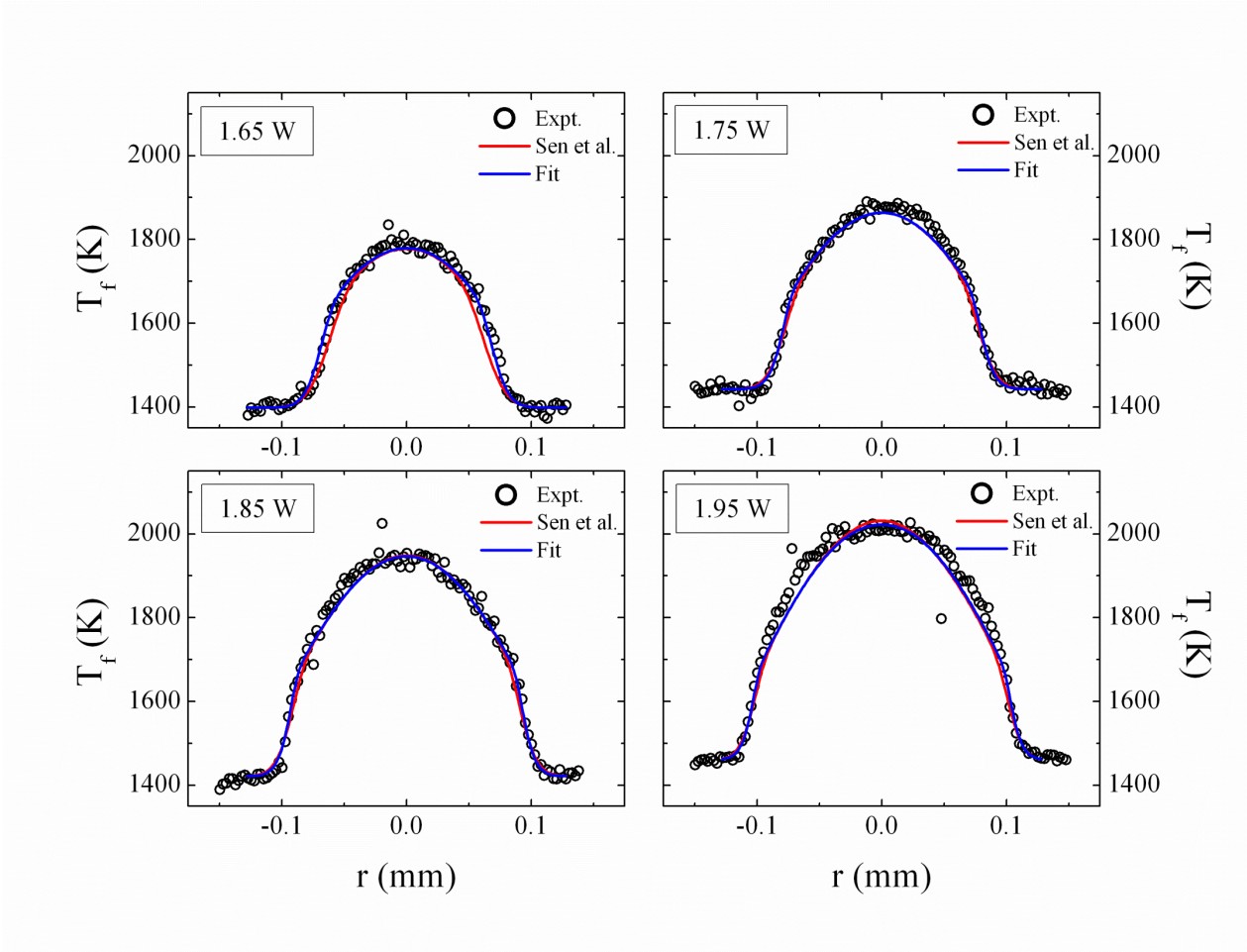
1.65 W
1.75 W
1.85 W
1.95 W
Expt.
Sen et al.
Fit
T_f (K)
r (mm)
2000
1800
1600
1400
-0.1
0.0
0.1

FIGURE 7

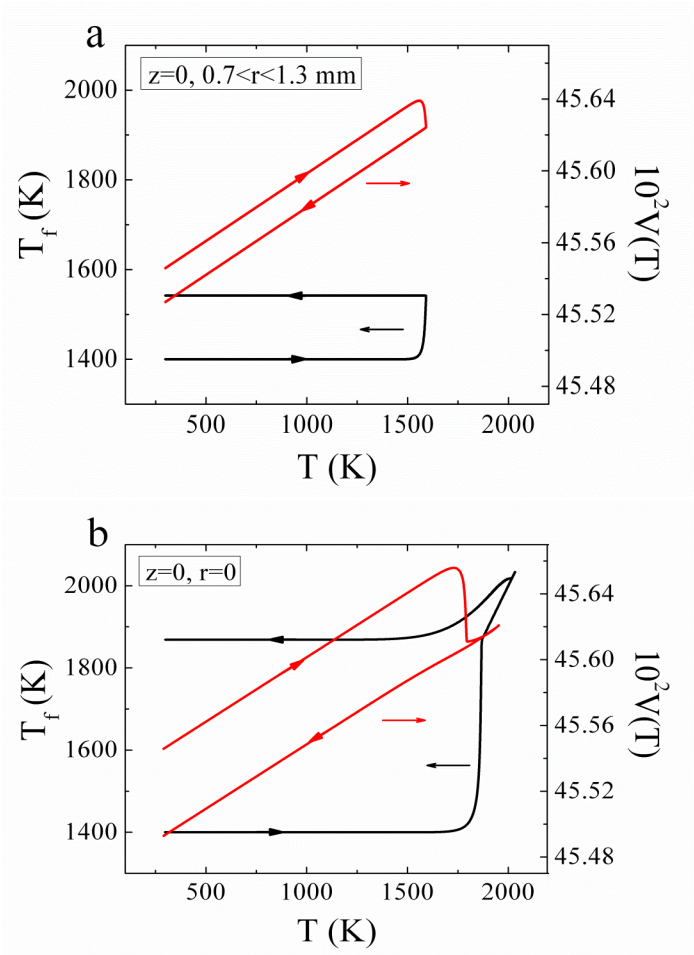
a
z=0, 0.7<r<1.3 mm
2000
1800
1600
1400
T_f (K)
45.64
45.60
45.56
45.52
45.48
$10^2V(T)$
500
1000
1500
2000
T (K)
b
z=0, r=0
2000
1800
1600
1400
T_f (K)
45.64
45.60
45.56
45.52
45.48
$10^2V(T)$
500
1000
1500
2000
T (K)

FIGURE 8

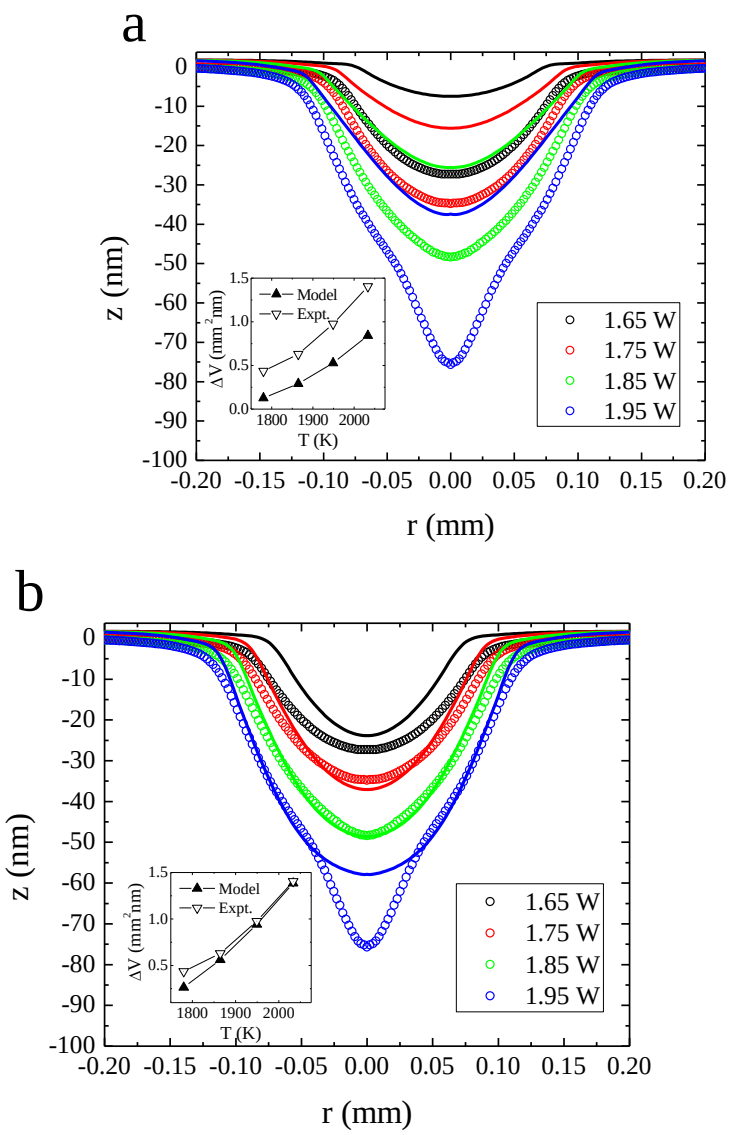
a
z (nm)
r (mm)
1.65 W
1.75 W
1.85 W
1.95 W
Model
Expt.
ΔV (mm³nm)
T (K)
b
z (nm)
r (mm)
1.65 W
1.75 W
1.85 W
1.95 W
Model
Expt.
ΔV (mm³nm)
T (K)

FIGURE 9

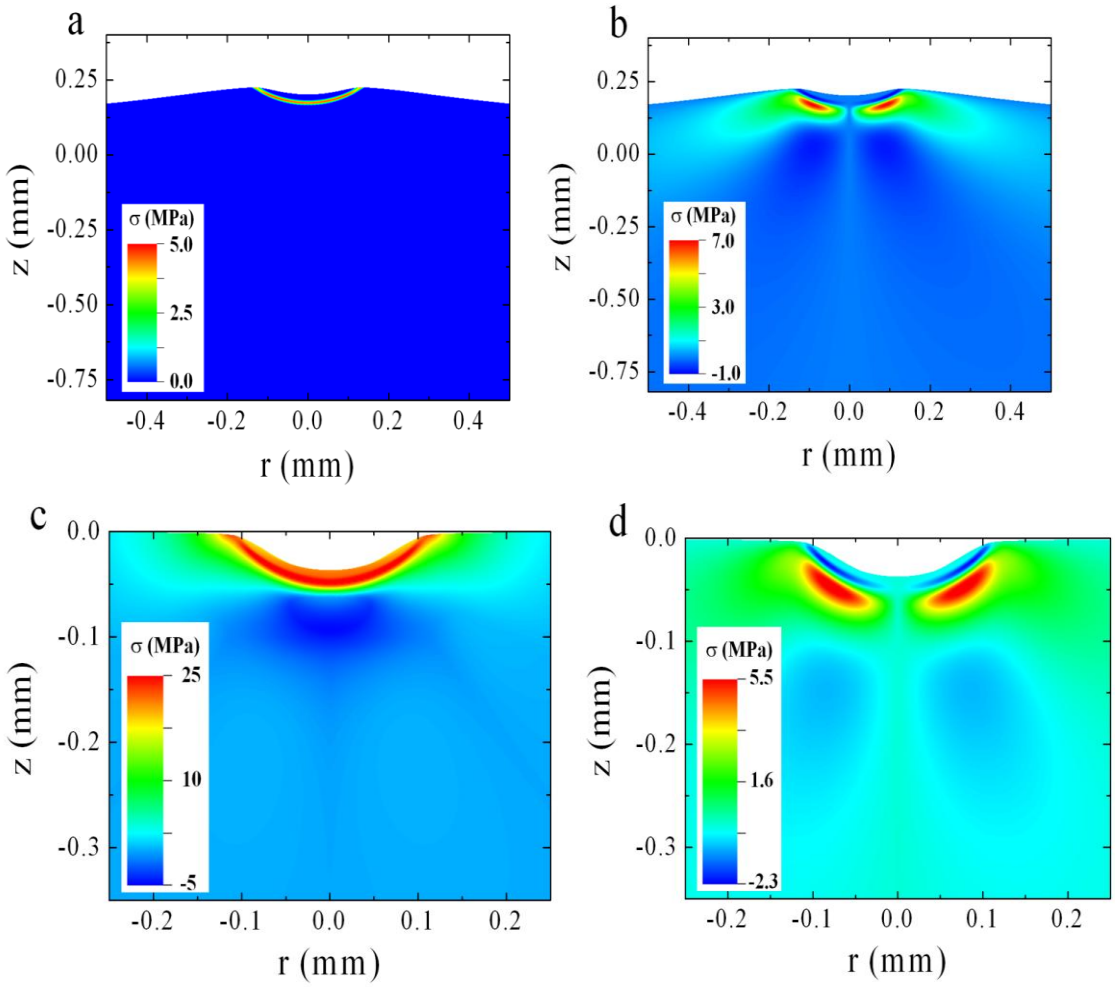

FIGURE 10

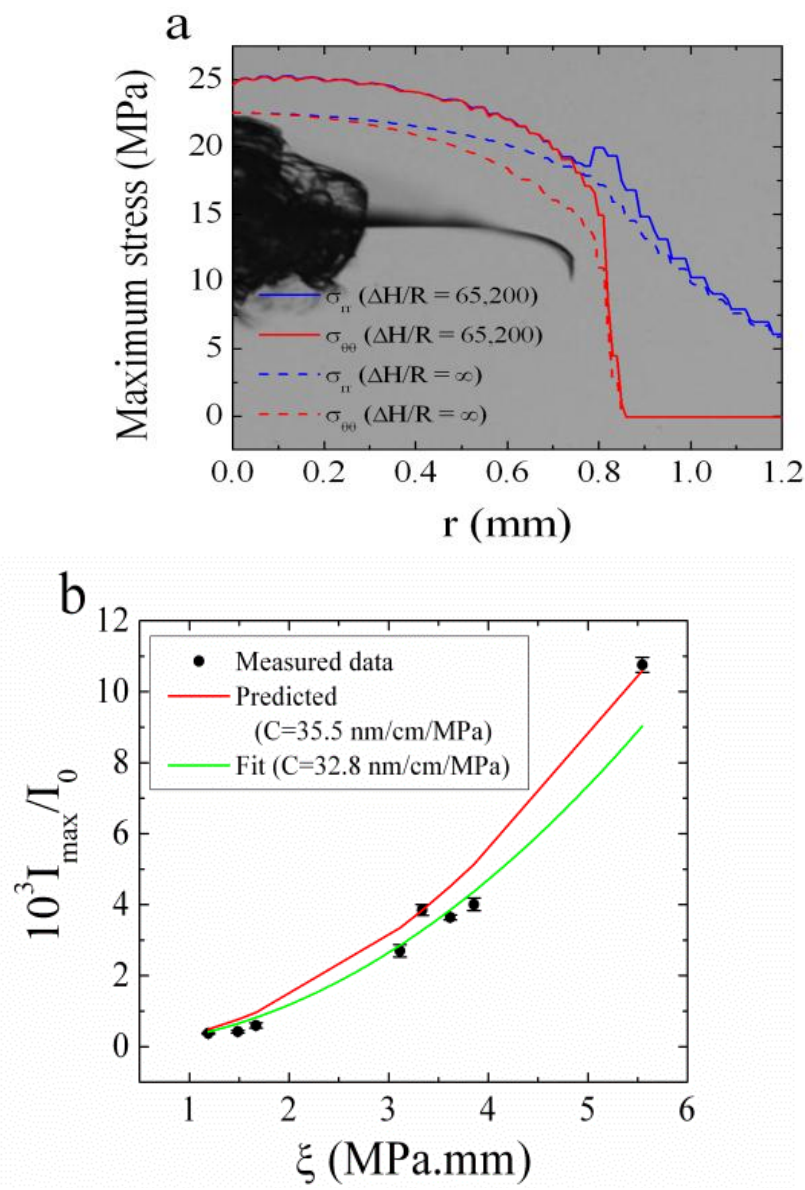
a
Maximum stress (MPa)
r (mm)
σrr (ΔH/R = 65,200)
σθθ (ΔH/R = 65,200)
σrr (ΔH/R = ∞)
σθθ (ΔH/R = ∞)
b
Measured data
Predicted
(C=35.5 nm/cm/MPa)
Fit (C=32.8 nm/cm/MPa)
10³Imax/I0
ξ (MPa.mm)

FIGURE 11

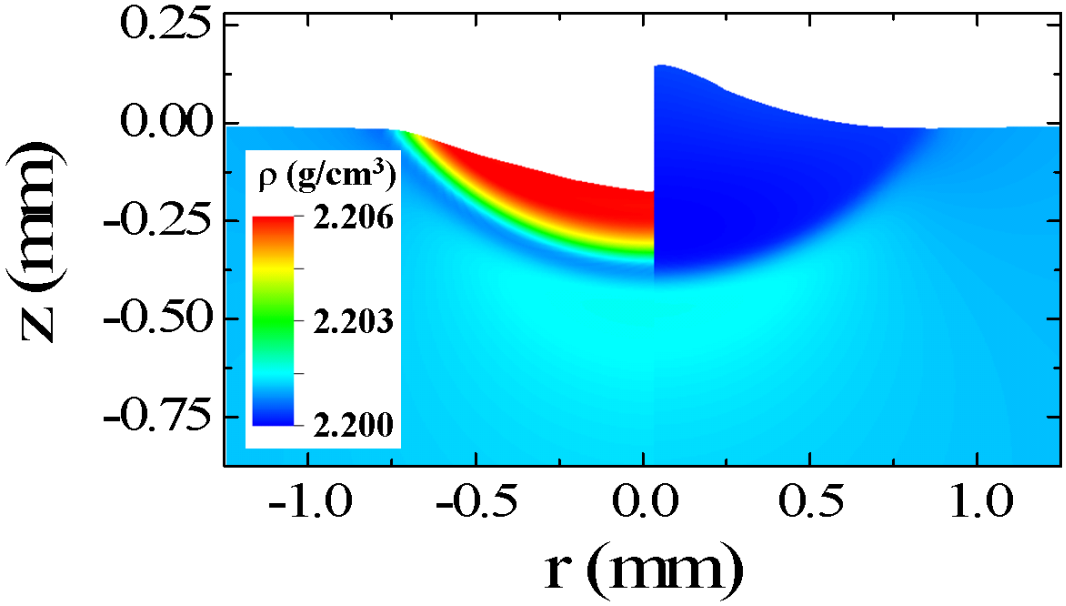

FIGURE 12